Determination of Parameters Characteristic of Dynamic Weakening Mechanisms During Seismic Faulting in Cohesive Rocks

C. Cornelio, E. Spagnuolo, S. Aretusini, S. Nielsen, F. Passelègue, M. Violay, M. Cocco, G. Di Toro

To cite this version:

C. Cornelio, E. Spagnuolo, S. Aretusini, S. Nielsen, F. Passelègue, et al.. Determination of Parameters Characteristic of Dynamic Weakening Mechanisms During Seismic Faulting in Cohesive Rocks. Journal of Geophysical Research : Solid Earth, 2022, 127, 10.1029/2022JB024356 . insu-03869596

HAL Id: insu-03869596
https://insu.hal.science/insu-03869596v1

Submitted on 24 Nov 2022

JGR Solid Earth

RESEARCH ARTICLE
10.1029/2022JB024356

Key Points:

- A data set of ∼100 experiments was used to explore the possible activated weakening mechanisms under a broad range of deformation conditions
- Constitutive parameters of the weakening models were obtained using a non linear norm-based optimization procedure
- A composite model with two weakening mechanisms is discussed to interpret the shear stress evolution with slip in different slip ranges

Supporting Information:

Supporting Information may be found in the online version of this article.

Correspondence to:

C. Cornelio,
chiara.cornelio@ingv.it

Citation:

Cornelio, C., Spagnuolo, E., Aretusini, S., Nielsen, S., Passelègue, F., Violay, M., et al. (2022). Determination of parameters characteristic of dynamic weakening mechanisms during seismic faulting in cohesive rocks. *Journal of Geophysical Research: Solid Earth*, *127*, e2022JB024356. https://doi.org/10.1029/2022JB024356

Received 9 MAR 2022
Accepted 28 JUN 2022

Determination of Parameters Characteristic of Dynamic Weakening Mechanisms During Seismic Faulting in Cohesive Rocks

C. Cornelio[1], E. Spagnuolo[1], S. Aretusini[1], S. Nielsen[2], F. Passelègue[3], M. Violay[4], M. Cocco[1], and G. Di Toro[1,5]

[1]HP-HT Laboratory, Istituto nazionale di Geofisica e Vulcanologia, Rome, Italy, [2]Department of Earth Sciences, Durham University, Durham, UK, [3]Geoazur, CNRS, Université Cote d'Azur, Valbonne, France, [4]Laboratory of Experimental Rock Mechanics EPFL, Lausanne, Switzerland, [5]Dipartimento di Geoscienze, Università degli Studi di Padova, Padua, Italy

Abstract While sliding at seismic slip-rates of ∼1 m/s, natural faults undergo an abrupt decrease of shear stress called dynamic weakening. Asperity-scale (<<mm) processes related to flash heating and weakening and, meso-scale (mm-cm) processes involving shear across the bulk slip-zone, related to frictional melting or viscous flow of minerals, have been invoked to explain pronounced velocity-dependent weakening. Here we present a compilation of ∼100 experiments performed with two rotary shear apparatuses. Cohesive rock cylinders of basalt, gabbro, granitoid rocks and calcitic marble were sheared at various values of effective normal stress ($\sigma_{neff} = 5$–40 MPa), target slip-rate ($V_t = 0.1$–6.5 m/s) and fluid pressure ($P_f = 0$–15 MPa). To account for the uncertainties of constitutive parameters, we introduce a norm-based optimization procedure on a set of model parameters by comparing the shear stress evolution inferred from the proposed weakening models with the shear stress measured during the experiments. We analyze the fit to experimental data of each weakening model and we discuss a composite model in which two weakening mechanisms (namely flash heating and bulk melting, flash heating and dislocation/diffusion creep) are used to test the hypothesis that they match the shear stress evolution in different slip ranges. We found that for slip smaller than a slip-switch distance $\delta_{0,}$ the weakening is better described by mechanisms occurring at the asperity scale whereas for larger slip values the bulk model performs better. The inferred δ_0 values decrease with normal stress suggesting that during earthquakes bulk mechanisms can govern shear stress evolution after a few centimeters of slip.

Plain Language Summary During earthquakes faults undergo to rapid slip caused by shear stress evolution from an initial value to the peak stress followed by a sharp decrease to residual stress level. This evolution is determined by fault frictional properties. The drop in shear stress defines the so-called dynamic weakening. We analyze the shear stress evolution inferred from many laboratory experiments performed on four lithologies and a range of experimental conditions. We match the stress evolution with slip using different constitutive models to interpret dynamic weakening processes. We constrain both uncertainties and range of variability of constitutive parameters using a statistical optimization procedure. The proposed weakening models represent both micro-scale (∼mm) and meso-scale (∼cm) processes involving heating and weakening at the asperity contacts and across the bulk slip-zone, respectively. The analysis of the fit to experimental data inferred from different weakening models allowed us to discuss a composite model in which asperity-scale processes precede bulk-scale processes matching shear stress evolution in different slip ranges. The transition from asperity-scale to bulk-scale mechanism defines the slip-switch distance, which depends on the stress applied on the experimental fault. Our results shows that bulk-scale mechanisms can govern the fault frictional response after relatively small values of slip.

1. Introduction

Earthquakes are certainly one of the most important manifestations of faulting and the understanding of dynamic fault weakening during the initiation and the propagation of a seismic rupture is a major task for geoscientists. In particular, understanding how shear stress varies with slip is still a key challenge to tackle in order to interpret the mechanisms governing dynamic fault weakening during earthquakes (Rice, 2006). Earthquake ruptures propagate at speeds of ∼km/s reaching slip-rates of ∼1 m/s within the fault zone at depth in the Earth's crust (Heaton, 1990; Rice & Cocco, 2007). Under these quite extreme deformation conditions, fault rocks experience an abrupt temperature increase due to frictional heating and fault shear stress decreases with increasing slip velocity and slip (Di Toro et al., 2011; Rice, 2006). Several physical and chemical processes have been proposed to be associated with this reduction in fault strength (Tullis, 2015). In fact, during seismic slip, depending on the composition of the rock and the presence of fluids, fault wear and frictional heating result in (a) flash heating at the asperity (micro-)scale contacts of the rubbing surfaces (Goldsby & Tullis, 2011; Rice, 2006), (b) grain-size reduction producing nm-sized particles (Sammis & Ben-Zion, 2008; Siman-Tov et al., 2013; Tisato et al., 2012), (c) mineral breakdown and amorphization, and/or formation of new minerals via processes such as: decarbonation in calcite- and dolomite-built rocks, dehydroxylation and amorphization in clays (Aretusini et al., 2017, 2019; Brantut et al., 2008; Han et al., 2007; Martinelli & Plescia, 2004) or graphitization of amorphous carbon (Kuo et al., 2014), (d) phase changes such as the transition, especially in silicate-built rocks, from solid to melt (Sibson, 1975; Spray, 1995) or, in the case of fluids, from liquid to vapor or supercritical states (Acosta et al., 2018; J. Chen et al., 2017). These peculiar and transient fault products or, in the presence of pore fluids, their interaction with the solid matrix, may activate many dynamic weakening mechanisms. For instance, in the case of silicate-built rocks, frictional melts may lubricate the fault (Di Toro, Hirose, Nielsen, Pennacchioni, & Shimamato, 2006; Hirose & Shimamoto, 2005; Tsutsumi & Shimamoto, 1997). Alternatively, the formation and presence of nanoparticles may trigger grain-size- and temperature-dependent deformation weakening mechanisms, like grain boundary sliding aided by diffusion creep (De Paola et al., 2015; Green et al., 2015; Pozzi et al., 2021; Rowe et al., 2019; Spagnuolo et al., 2015). The release of volatiles due to dehydroxylation of clays or the thermal expansion of preexisting pore fluids may result in the pressurization and weakening of the fault (Ferri et al., 2010; Sibson, 1973). Moreover, the abrupt coseismic compaction of fluid-saturated gouges may result in mechanical pressurization of the trapped fluids and fault weakening (Aretusini, Meneghini, et al., 2021; Faulkner et al., 2018). However, though it is recognized that dynamic fault weakening is due to both thermally and mechanically activated processes (flash heating, bulk melting, thermal pressurization, viscous flow, etc.) the efficiency of any of these weakening mechanisms is debated and it might be assumed that mechanisms occurring at different temporal and spatial scales control different stages of the weakening phase (Nielsen et al., 2021).

Our knowledge on microscale processes has been improved with the description of the internal structure of the fault zone (Caine et al., 1996; Faulkner et al., 2011). Indeed, the definition of the fault zone structure is essential to interpret and distinguish the chemical and physical processes controlling dynamic weakening. In fact, coseismic slip often occurs on a sub-centimeter thick principal slipping zone (PSZ) (Austrheim & Boundy, 1994; Boullier et al., 2001; Chester & Chester, 1998; Di Toro et al., 2005; Sibson, 2003), embedded in a shearing zone (fault core) surrounded by a broad damage zone. There is a general agreement that dynamic weakening mechanisms can be grouped by those occurring at the scale of the asperities in the early slip stages, when shear stress is around its peak value and are activated at the scale of the asperities and those occurring within the bulk of the PSZ (Pozzi et al., 2019; Rice, 2006; Violay et al., 2015) (Figure 1).

In this study, we analyzed results from laboratory experiments for a simplified fault zone analog, consisting of solid pre-cut cylinders put in frictional contact and sheared at high slip-rates (up to 6.5 m/s), to simulate seismic slip on a thin PSZ.

The aim of this study is to propose a statistical approach to investigate both the efficiency of one or more weakening mechanisms and the variability of the parameters in their respective ranges. Here we use an optimization procedure which, based on a few a priori assumptions, explores the parameter space and realizes the best fit of the experimental data. Therefore, for the goal of this study, it is useful to briefly introduce and discuss the analytical formulation of some of the most relevant dynamic weakening mechanisms proposed in the literature. Moreover, it is useful to describe and identify the parameters that we will vary in a range previously defined in literature. The analytical formulation and the parameters definition were, in most cases, first proposed in theoretical models and then tested in dedicated laboratory experiments.

Flash heating and weakening is based on the observation that fault asperity contacts constitute the real area of contact between two sliding surfaces (Archard, 1958) (Figure 1a). Asperities sustain a high contact stress and during seismic slip, they have an intense, highly localized, heating (Rice, 2006). The produced heat is proportional to the contact lifetime, slip-rate and contact stress. The contact frictional strength decreases by thermal degradation of the asperities. The degradation of numerous asperities determines the reduction of the bulk fault strength. The first model of flash heating applied to earthquake mechanics was proposed by Rice (1999, 2006). In this model, the asperity contacts are assumed to last over a uniform slip distance D_{FH} (i.e., with uniform lifetime

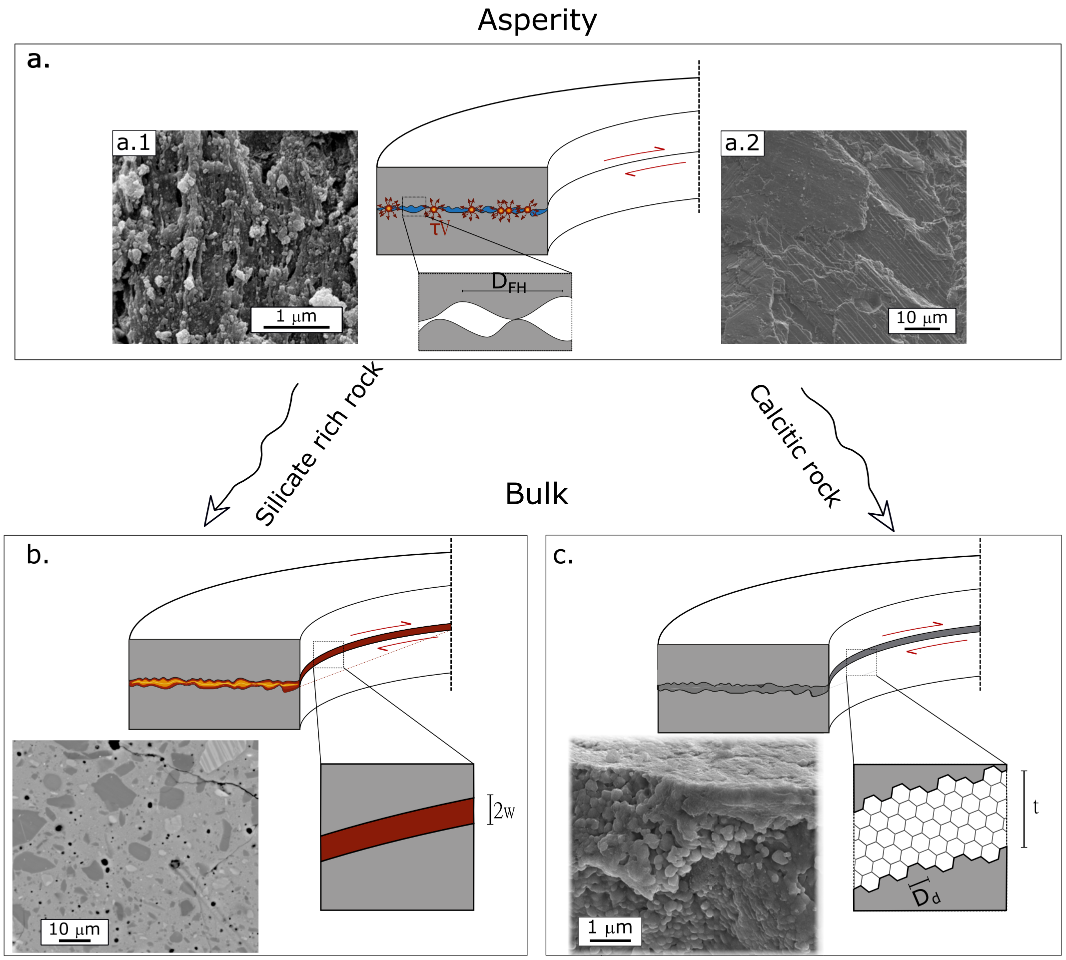

Figure 1. Schematic representation of the experimental fault and interpretation of the transition between asperity-scale and bulk-principal slipping zone (PSZ)-scale dynamic weakening mechanisms characterizing the composite model investigated in this study. Panel (a): During the first stage of the experiments, dynamic weakening is controlled by asperity-scale processes (flash heating) and temperature rises at the asperity contacts. For silicate-built rocks, the asperities start to melt (panels (a1 and b)), while for calcite-built rocks, nm-sized grains (i.e., nanograins or nanoparticles) characterize the PSZ (panels (a2 and c)). Due to frictional heating, temperature continue to increase in the extremely thin PSZ: bulk weakening mechanisms are activated by frictional melting for the (b) silicate-built rocks and diffusion creep for (c) calcite-built rocks. D_{FH} is the asperity size and D_D is the grain size; 2w is the thickness of the slipping zone.

D_{FH}/V, where V is the slip-rate), and to have a constant shear strength τ_c at low temperature. Once an asperity contact achieves a weakening temperature T_w, its shear strength vanishes. The weakening temperature is specific of the rock mineralogical composition. It can be shown that T_w is achieved at a critical slip-rate V_w, and that as slip-rate increases above V_w the lifetime of each asperity gradually decreases. Consequently, when $V < V_w$, no weakening will occur, but at $V > V_w$, the fault undergoes dynamic weakening, where shear stress is inversely proportional to V. The model can be represented by the system of equations (Equation 1):

$$\tau_{FH} = \begin{cases} \tau_s = \mu_s \sigma'_n & \text{if } V \le V_w \\ \tau_w = \left[(\mu_s - \mu_{dyn})\dfrac{V_w}{V} + \mu_{dyn}\right]\sigma'_n & \text{if } V > V_w \end{cases} \qquad (1)$$

with μ_s static friction coefficient, μ_{dyn} dynamic friction coefficient and σ'_n effective normal stress. The effective normal stress is the difference between the normal stress σ_n and fluid pressure P_f. The critical velocity weakening V_w is defined as (Rice, 2006):

$$V_w = \frac{\pi \alpha_{th}}{D_{FH}} \left[\frac{\rho C_p \left(T_w - T_f \right)}{\tau_c} \right]^2 \tag{2}$$

with α_{th} thermal diffusivity (Table S5 in Supporting Information S1), ρC_p rock specific heat per unit volume, T_f average (or bulk) temperature and D_{FH} the asperity diameter (i.e., the slip asperity interaction distance). The parameters T_w, α_{th}, ρ and C_p are lithology-dependent. In this model, the τ_c is the normal stress borne by contacts and it is approximately equal to the indentation hardness (H_0) of the minerals constituting the rocks multiplied by the coefficient of friction obtained at low slip-rate (μ_0) $\tau_c = \mu_0 * H_0$ (Goldsby & Tullis, 2011). However, the hardness can be considered proportional to the asperity size D_{FH} (Evans & Goetze, 1979).

This theoretical model has been enhanced by further studies, which consider a fractal distribution of the asperities, or the possible activation of flash heating and weakening in the presence of fluids (Acosta et al., 2018; Beeler et al., 2008; Brantut & Platt, 2017; Platt et al., 2015; Violay et al., 2014). In Goldsby and Tullis (2011), they measured V_w in dedicated experiments for many rock types to be in the range between 0.1 and 0.5 m/s. Additional laboratory experiments imposing high slip-rate on rock surfaces corroborated the role of flash heating in controlling the decrease of friction coefficient at $V > V_w$ (Hirose & Shimamoto, 2005; Passelègue et al., 2014; Proctor et al., 2014). Very few experimentally-based studies focused so far on the role of ambient conditions such as ambient temperature (Noda, 2008; Passelègue et al., 2014) or presence of water (Acosta et al., 2018; Violay et al., 2014), and on the microphysical processes associated with flash heating and weakening such as intra-lattice dislocation avalanches and lattice breakdown (Spagnuolo et al., 2015).

Bulk melting lubrication is probably the only weakening mechanism supported by sound field, experimental and theoretical evidence (Fialko & Khazan, 2005; Nielsen et al., 2008; Sibson et al., 1975; Spray, 1995). The activation of this mechanism involves the frictional melting of silicate minerals in the PSZ and wall rock to form, once solidified, a rock called pseudotachylyte (Sibson, 1975; Spray, 1995) (Figure 1b) To date, tectonic pseudotachylytes are considered the only reliable markers of ancient seismic slip in exhumed faults (Cowan, 1999; Rowe & Griffith, 2015). The transition from initial flash heating and weakening to bulk melting lubrication for experiments on cohesive silicate-built rocks, is quite complex (Hirose & Shimamoto, 2005). The transition is a function of the mineral composition, normal stress, ambient condition, slip acceleration and target slip-rate (Del Gaudio et al., 2009; Hirose & Shimamoto, 2005; Hung et al., 2019; Niemeijer et al., 2011). During simulated seismic slip, after the initial shear stress decrease caused by flash heating, dynamic shear stress increases again due to the formation of isolated, clast-laden, low temperature, and highly viscous melt patches (Hirose & Shimamoto, 2005; Hung et al., 2019). Once the isolated melt patches are linked to form a continuous melt layer, full lubrication occurs and fault strength is controlled by the temperature, clast content, composition, melt/boundary geometry etc. of the melt layer (Nielsen, Di Toro, & Griffith, 2010; Nielsen et al., 2008); see also video with high speed infrared camera in (Niemeijer et al., 2011)) and the shear stress is

$$\tau = \frac{\eta V}{2w} \tag{3}$$

with η the viscosity, V the slip-rate, and $2w$ the thickness of the melt layer (Figure 1b). Importantly, the complex initial evolution is observed usually in experiments performed at normal stresses <5 MPa and "disappears" at larger normal stress and for high slip acceleration or high power density (PD, the product of τ and V) (Violay et al., 2014). In the presence of fluids, flash heating and bulk melting are still observed in gabbro (Violay et al., 2014), basalt (Violay et al., 2015), and granitoid rocks (Acosta et al., 2018; Cornelio et al., 2019; Passelègue, Spagnuolo, et al., 2016). However, the presence of liquid water has a cooling effect on the asperities and on the entire slip surface and results in a delay in the formation of a continuous melt layer (Violay et al., 2014).

Viscous flow mechanisms, such as high-temperature diffusion creep and dislocation creep, may result in low shear stress at high strain rate (Demurtas et al., 2019; De Paola et al., 2015; Green et al., 2015; Pozzi et al., 2021; Verberne et al., 2014), especially with increasing temperature and decreasing grain size. The decrease in grain size results by a combination of wear and mineral breakdown due, for instance, to decarbonation. In carbonate-built (calcitic and dolomitic marble) rocks sheared at seismic slip-rates, shear stress was shown to be independent of normal stress but strongly dependent on strain rate, suggesting that crystal-plastic processes might be active (Figure 1c). In Pozzi et al. (2019), they suggested that diffusion creep can also occur without mineral breakdown (i.e., decarbonation), being solely enhanced by the grain-size reduction during sliding. Dislocation creep and diffusion creep are modeled with the constitutive flow law (Poirier, 1995):

$$\tau_D = \left(\frac{\dot{\gamma}}{A D_d^{-b} e^{-\frac{H}{RT}}} \right)^{\frac{1}{n}} \tag{4}$$

with $\dot{\gamma}$ being the shear strain rate, defined as V/t, where t is two times the PSZ thickness, A is the pre-exponential factor, H the apparent activation energy for creep, R the gas constant, T the absolute temperature, τ the shear stress, n the stress exponent, D_D the grain size and b the grain size exponent.

Although it cannot be considered a dynamic weakening mechanism in itself, decarbonation or the thermal (and possibly mechanical (Italiano et al., 2008; Martinelli & Plescia, 2004)) breakdown of carbonate minerals (calcite, dolomite, etc.), is often concomitant to the large dynamic weakening of sliding rock surfaces (Brantut et al., 2008; Han et al., 2007). During seismic slip, frictional heating causes the decomposition of calcite ($CaCO_3$) into lime (CaO) and CO_2 (Han et al., 2007). This decarbonation reaction should occur at bulk temperatures ranging between 700 and 900°C (Rodriguez-Navarro et al., 2009). Similarly, dolomite decomposes in a breakdown reaction into lime (CaO), periclase (MgO) and CO_2 (temperature between 650 and 900°C) (Rodriguez-Navarro et al., 2012). All these reactions are endothermic: they buffer the temperature increase in the PSZ (Brantut et al., 2010; Sulem & Famin, 2009), and result in the transformation of original calcite or dolomite crystals in porous aggregates of CaO or CaO + MgO nanoparticles. While nanoparticles do not directly lubricate the experimental fault, they allow the activation of temperature- and grain size-dependent (e.g., grain boundary sliding aided by diffusion creep) deformation mechanisms (Green et al., 2015). For instance, in the case of cohesive calcitic marbles, the very early stages of simulated seismic slip and dynamic weakening are associated to the release of gases (H_2, CO_2 and CH_4 where the occurrence of hydrogen H is related to the breakdown of H_2O adsorbed on the rock surfaces) and to "flash" amorphization (Spagnuolo et al., 2015). The bulk temperature in these experiments was estimated in a range of 25–30°C. However, higher temperatures can be achieved for stress localization at the small size of the contact asperities or because of thermal effects due to dislocation motion (possibly moving at sonic speeds) inside the calcite crystals (Spagnuolo et al., 2015). The eventual pressurization of the gases released during decarbonation and the consequent decrease in effective stress and weakening within the fault asperity contacts or bulk PSZ has also been debated in literature (Sulem & Famin, 2009).

In the literature, many other mechanisms were invoked to explain the decrease of fault shear strength with co-seismic slip. Among them: thermal pressurization (Rice, 2006; Sibson, 1973) (Text S1 in Supporting Information S1), elastohydrodynamic lubrication (Brodsky & Kanamori, 2001; Cornelio et al., 2019, 2020) and powder lubrication (Han et al., 2010; Reches & Lockner, 2010; Tisato et al., 2012). There is a general agreement that multiple weakening mechanisms can coexist, contributing or competing in controlling dynamic fault weakening. This makes the study of the coseismic slip more complex, since multiple processes might involve many spatial and temporal scales (Cocco & Tinti, 2008; Cocco et al., 2016) and it is challenging to distinguish the dominant weakening mechanism during the experiments (De Paola et al., 2015; Tsutsumi & Shimamoto, 1997).

All the mechanisms previously described are characterized by numerous parameters, depending on the fault rock composition (silicate-built, carbonate-built, etc.), the loading (i.e., normal stress, slip acceleration, etc.) and ambient conditions (presence and composition of fluids, fluid pressure). These conditions have a pivotal role in the activation of a specific type of weakening mechanism, at the asperity scale and at the bulk PSZ scale. Moreover, finding a set of parameters, which satisfy the constitutive laws presented above (Table 1), while constraining their significance and their range of variability, requires a systematic comparison of experimental data and modeling results for each parameters set, an operation which rarely appears in previous studies. Finally, assuming that several weakening mechanisms can coexist during the weakening stage implies the modeling of a transition from a weakening mechanism to another one, as slip progresses. For instance, if flash heating of asperity contacts is preceding other types of bulk deformation processes, such as those described above (Table 1), the transition between these two mechanisms might be identified in the evolution of shear stress with slip and possibly modeled.

In this work, we use the optimization algorithm to explore the parameter space, constrain the range of variability of constitutive parameters, and infer their uncertainties under seismic experimental conditions. We use the optimized parameters to fit the experimental data using a composed approach which allows, if needed, to comprise two weakening mechanisms (i.e., flash heating, bulk melting and viscous flow mechanisms) that best

Table 1

Weakening Mechanisms Investigated in This Study and Main Parameters of the Modeling Approach

Weakening mechanism	Optimized parameters	Not optimized parameters	Lithology	ExperimentalConditions	Equations
Flash heating	D_H, μ_p, μ_s	T_w	All	RH, Pf	$\tau_{FH} = \begin{cases} \tau_s = \mu_s \sigma_n & \text{if } V < V_w \\ \tau_w = \left[\left(\mu_s - \mu_{dyn} \right) \frac{V_w}{V} + \mu_{dyn} \right] \sigma_n & \text{if } V > V_w \end{cases}$ 1
Bulk melting	K factor	$T_m = T_w$	Basalt, gabbro, granitoid	RH, Pf	$\tau = \frac{\eta V}{2w}$ 3
Diffusion creep	D_D, t, b	A, H, n	Calcitic marble	RH, Pf	$\tau_D = \left(\frac{\dot{\gamma}}{A D_d^{-b} e^{-\frac{H}{RT}}} \right)^{\frac{1}{n}}$ 4
Dislocation creep	D_D, t, n	A, H, b	Calcitic marble	RH, Pf	$\tau_D = \left(\frac{\dot{\gamma}}{A D_d^{-b} e^{-\frac{H}{RT}}} \right)^{\frac{1}{n}}$ 4

Note. For each weakening mechanism, the table reports the optimized and not optimized parameters, the analyzed lithology and the experimental conditions (RH for room humidity, Pf for fluid pressurized experiments) and the constitutive law for computing the shear stress. *T*, Temperature dependent; R, F, rock or fluid properties.

fit the data in a given slip range. We analyze data resulting from a large set of laboratory experiments performed on silicate-built and calcite-built rocks. Flash heating and bulk melting are investigated for silicate-built rocks, while flash heating and dislocation creep or flash heating and diffusion creep are investigated for calcite-built rocks. Furthermore, we present a novel way to model and interpret the measured temperature at high acquisition rates with optical fibers inside the slipping zone (Aretusini, Núñez-Cascajero, et al., 2021). This approach helps to validate the assumptions made when modeling temperature from the mechanical data and interpret the possible contribution to the temperature rise of the investigated weakening mechanism. Among the weakening mechanisms discussed in the literature, thermal pressurization (Rice, 2006; Sibson, 1973) has been largely used to explain the fault dynamic weakening stage in theoretical models (Andrews, 2002; Noda & Lapusta, 2013). However, the discussion of thermal pressurization is outside the scope of the present paper for the large number of unknowns, which make the system of equations undetermined and our optimization method applicable with limitations. Indeed, the values of the considered parameters are rarely available in literature and it is not easy to constrain them from high velocity frictional experiments performed so far. Despite these limitations, some relevant aspects from attempted inversions are reported in Text S1 in Supporting Information S1. The overarching ambition of our work is to shed light on dynamic weakening mechanisms and to constrain constitutive parameters to be included in physically- and geologically-based dynamic earthquake rupture simulations (Gabriel et al., 2012; Murphy et al., 2018; Tinti et al., 2021).

2. Experimental Data

We have built a comprehensive data set of experimental data acquired in the last decade in laboratory experiments performed with the rotary shear machine SHIVA installed at the Istituto Nazionale di Geofisica e Vulcanologia in Rome (Table S1–S4 in Supporting Information S1) (Di Toro et al., 2010; Niemeijer et al., 2011). The experiments aim at reproducing the shear stress evolution with slip and time as well as dynamic weakening during earthquake slip propagation. We re-analyzed about one hundred experiments performed on solid pre-cut cylinders (50/30 mm or 50/0 mm external/internal diameter) of basalt (Violay et al., 2014), gabbro (Violay et al., 2014, 2015), granitoid rocks (Westerly granite (Cornelio et al., 2019; Passelègue, Schubnel, et al., 2016), tonalite (Castagna, 2012) and calcitic marble (Violay et al., 2014, 2015). Moreover, we also use the data from a few experiments performed on tonalite (same composition of the one deformed by (Castagna, 2012)) with the HVRFA machine installed in Kyoto University, Japan (Shimamoto & Tsutsumi, 1994). The description of the experimental configuration (i.e., the samples were solid cylinders with diameter of 22.5 mm and length of 22 mm) can be found in (Di Toro, Hirose, Nielsen, Pennacchioni, & Shimamato, 2006) and (Di Toro, Hirose, Nielsen, & Shimamoto, 2006). The chosen lithologies are (a) representative of typical seismogenic continental crust and (b) the endmembers for investigating the weakening mechanisms described in the introduction section.

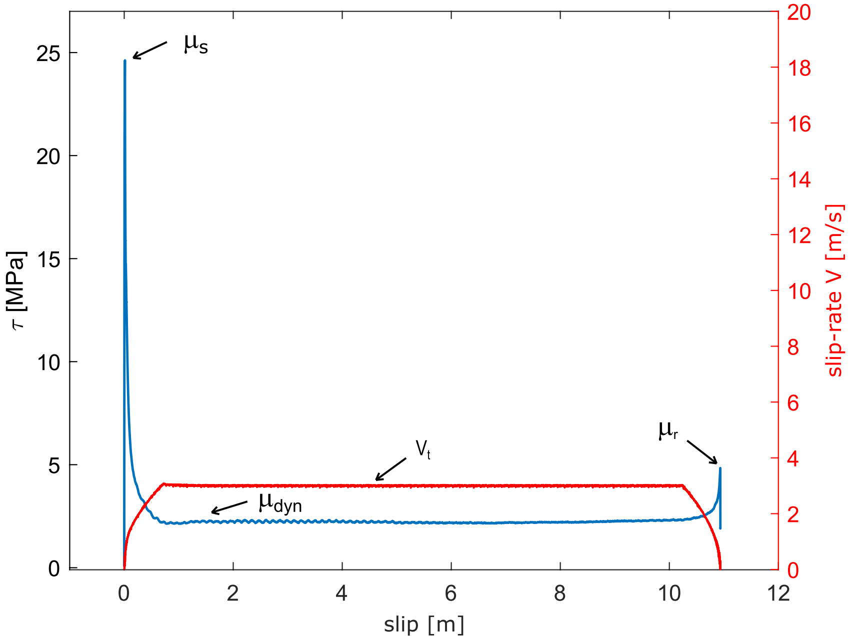

Figure 2. Result of a typical high velocity frictional experiment. Shear stress (blue curve) and imposed slip-rate V (red curve) are plotted as a function of slip for experiments s557 performed on gabbro under room humidity condition, normal stress of 30 MPa and $V_t = 3$ m/s. When the slip-rate function V is applied, the shear stress τ increases until the peak value (μ_s σ'_n), the static friction coefficient is overcome and slip suddenly increases. Immediately after the peak stress, the shear stress starts decreasing with slip up to a minimum (approximately steady state) value ($\mu_{dy}n\sigma'_n$). Finally, during the deceleration stage, the shear stress increased again up to a re-strengthening value ($\mu r\sigma'_n$).

The experiments reproducing seismic deformation conditions were performed by imposing a trapezoidal slip-rate function (Figure 2). The target slip-rate V_t ranges between 0.1 m/s and 6.5 m/s. The acceleration and deceleration ramps were usually equal for each experiment, ranging between 5.2 and 30.1 m/s^2. The effective normal stress was kept constant during each experiment, ranging between 5 and 40 MPa. In the experiments performed under drained pressurized water condition, the fluid pressure was kept constant during the experiments by a membrane pump and it ranged between 2.7 and 15 MPa. Mechanical data (axial load, torque, axial displacement and angular rotation) were acquired at a sampling rate between 250 Hz and 25 kHz, depending on the target slip-rate. Slip, slip-rate and shear stress were determined using the methods outlined in Niemeijer et al. (2011) and Tsutsumi and Shimamoto (1997). The original mechanical data were acquired with a constant time step (between 0.04 and 4 ms). We resampled our data to obtain a constant slip step of $\Delta x = 0.001$ m for all the experiments so that, during the fitting and optimization procedure, the data points during the acceleration stage are not overrepresented with respect to those during the plateau at constant velocity. This comprehensive data set offers a unique opportunity to integrate and discuss dynamic fault weakening mechanisms at high slip-rates for each lithology and loading conditions.

3. Methods

Depending on the lithology of rock samples, we model the shear stress evolution with slip inferred from laboratory experiments assuming that two mechanisms may intervene during the weakening stage. The two mechanisms are flash heating and dislocation/diffusion creep in carbonate rich rocks or flash heating and bulk melting in silicate rich rocks. Using the norm-based optimization approach on the performed experiments, we were able to constrain a set of optimized model parameters, for each weakening mechanisms considered in this study (Table 1), which best fit the experimental data for each lithology and loading condition.

The parameters space is constrained by considering the range of values proposed in the literature (i.e., D_{FH}, μ_s static friction coefficient, μ_{dyn} dynamic friction coefficient, n stress exponent, D_D grain size and b the grain size exponent) (Table 1). The goodness of the fit to experimental data is quantified through the squared norm value of the residuals (SNR). We use the retrieved SNR values to discuss the weakening mechanisms (e.g., flash heating and diffusion or dislocation creep for calcitic marble) and the fit to experimental data yielding the lowest SNR per lithology and loading condition. Moreover, we also allow a composition of the two models by identifying the slip ranges in which each weakening mechanism best matches the experimental data.

The shear stress is estimated with the constitutive equations proposed for each weakening mechanism (Equations 1–4) using the values for σ'_n, V and P_f of each experiment. The shear stress constitutive equation is fully coupled with the temperature increase, which is estimated using the heat diffusion equation. The fully coupled partial differential equations are solved using a 1D finite difference explicit method implemented in ®Matlab. This is an approximation of the cylindrical geometry, but the results do not differ substantially as discussed in (Nielsen, Mosca, et al., 2010). The model domain z is orthogonal to the fault plane, and it was discretized in 50 nodes equally spaced $\Delta z = 0.001$ m outside the melt layer w or slipping zone t (see Section 3.1 and 3.2). The melt layer and the slip zone t where discretized using $\Delta z = 1$ μm. Due to the symmetry of the experimental setup, we modeled only one-half of the sample assembly. In our model the fault is represented by a single point at $z = 0$. At each time iteration, the time step Δt was equal to $\Delta x/V(t)$.

With the only exception of the melt lubrication model (Section 3.1, Equation 12), the evolution of temperature T in the model domain and within the slipping zone was estimated using the heat diffusion equation (Carslaw & Jaeger, 1959):

$$\frac{\partial T}{\partial t} = \alpha_{th}\frac{\partial T}{\partial z^2} + Q \tag{5}$$

with α_{th} thermal diffusion, Q heat source:

$$\begin{cases} Q = \dfrac{1}{2}\dfrac{\tau(\delta)V(\delta)}{\rho C_p} \text{ in } z = 0; \\ \quad Q = 0 \quad \text{elsewhere} \end{cases} \tag{6}$$

with ρ rock density, C_p heat capacity, V slip-rate function and τ the modeled shear stress. The equation relating temperature and shear stress are mechanism-dependent and reported in the following sections.

Following Nielsen et al. (2021), the rock thermal diffusivity (α_{th}) and thermal conductivity $\left(\kappa = \frac{\alpha_{th}}{\rho C_p}\right)$ were considered temperature dependent, and the thermal dependence measured experimentally (Hartlieb et al., 2016; Merriman et al., 2018; Miao et al., 2014) was reproduced by adjusting the parameters of an empirical fit function:

$$\kappa = c_{c1}\exp\left(\frac{T}{c_{c2}}\right) + c_{c3} \tag{7}$$

$$\alpha_{th} = c_{a1}\exp\left(\frac{T}{c_{a2}}\right) + c_{a3} \tag{8}$$

The coefficients for thermal conductivity (c_{c1}, c_{c2}, c_{c3}) and thermal diffusivity (c_{a1}, c_{a2}, c_{a3}) are reported in Table S5 in Supporting Information S1. For experiments performed in presence of water, we considered an effective specific heat $(\rho C)_{eff} = ((1-\phi)\cdot\rho_r\cdot C_r) + (\phi\cdot\rho_w\cdot C_w)$ where r and w are related to the rock and to the water properties, respectively (Table S7 in Supporting Information S1).

We imposed an initial temperature $T = 298$ K in the entire domain. In the case of calcitic marble, optical fibers were used to measure the temperature at high spatial (ca. 20 μm) and temporal (1 kHz) resolution in the slipping zone (Aretusini, Núñez-Cascajero, et al., 2021). This new data set allowed us to discuss temperature estimates and the thermal control of the transition from flash heating to bulk-scale weakening processes (diffusion creep in that case).

In our formulation, for each set of experiments belonging to the different lithologies, the selected weakening mechanisms run in parallel to fit the curve representing the shear stress evolution with slip. For each model, the chosen parameters are optimized using an iterative procedure. The optimal model in the least-squares sense is obtained by minimizing the squared norm value of the residuals (SNR) defined as:

$$\min ||f(x)||_2^2 = \min \left(f_1(x)^2 + f_2(x)^2 + \ldots + f_n(x)^2 \right) \tag{9}$$

where $f_i(x)$ is the difference between the shear stress of the experimental data and the one obtained by the weakening model at the i-th slip step. The x vector contains the constitutive parameters to be optimized for each weakening mechanism. For each parameter, we impose the lower- and upper-limits and an initial guess value. To obtain the minimum of the function in Equation 9, we use the "trust-region-reflective Algorithm" (Sorensen, 1982). The iterative optimization is stopped when one of the stopping criteria is achieved (see Table S6 in Supporting Information S1). Each optimization attempt provides a set of optimized model parameters and the SNR. For a stable optimization procedure, the squared norm value has to decrease at each optimization iteration (Figure S1 in Supporting Information S1). To obtain a stable solution of the optimization procedure, the number of optimized parameters is kept small (maximum 3 for each investigated weakening model) and the number of possible mechanisms in the composite model were limited to two. Considering a third constitutive equation, for example, flash heating and diffusion creep associated with decarbonation, would require the optimization of at least two additional parameters with the consequence of increasing computational time without benefits for the goodness of the fit (Text S2 in Supporting Information S1).

The composite model is constructed by identifying the weakening mechanism that leads to the lowest residual (i.e., the difference between the observed shear stress τ_{data} and the modeled shear stress τ_m) for a range of slip values and that consequently better reproduces the experimental data in this range among all the considered mechanisms. Once the composite model is assembled, by putting together the two weakening mechanisms yielding the lowest residuals for two adjacent intervals of slip values, we use it to run a further parameter search and infer the final optimized parameters. We define the "slip-switch distance" as the slip value at which we infer the transition between the two best-fitting weakening mechanisms considered in each composite model. This transition can be interpreted as the slip distance at which the processes involving the bulk within the slipping zone overcome processes occurring at asperity contacts (Hirose & Shimamoto, 2005; Spagnuolo et al., 2015; Violay et al., 2014). This slip-switch is inferred for each lithology, loading and normal stress conditions. The composite model is here proposed to discuss and interpret the capacity of a single weakening mechanism to reproduce the shear stress evolution over the entire range of inferred slip values. The significance of the proposed approach relies on the capability of this composite model of identifying a range of slip values where one of the two selected processes is governing the frictional response and the shear stress evolution, as well as to study the parameters which best represent the dynamic weakening stage during specific slip ranges. Proposing the composite model as the best fitting solution to model shear stress evolution with slip is beyond the goals of this study.

3.1. Flash Heating and Bulk Melting Model

For the silicate-built rocks analyzed in this work (gabbro, basalt, granite and tonalite), the investigated weakening mechanisms are flash heating and bulk melting. Bulk melting can be only active when the temperature is higher than the rock melting temperature ($T > T_w$), whereas flash heating can be active at lower temperature $T < T_w$. It is therefore reasonable to assume that dynamic weakening is governed by flash heating for $T < T_w$ and by bulk melting for $T > T_w$. In other words, the two weakening mechanisms are sequential, because flash heating is necessary to activate bulk melting. Here, in the composed model, $T > T_w$ is a condition necessary but not sufficient for the activation of the bulk melting.

The flash heating is described by Equations 1 and 2. The parameters T_w, α_{th}, ρ and C_p are lithology dependent. ρ and C_p are kept constant, and the corresponding values are reported in Table S7 in Supporting Information S1. In this work, we will consider τ_c as a lithology dependent constant parameter and independent of D_{FH} (Table S7 in Supporting Information S1) to reduce the number of unknowns. Parameters μ_s, μ_{dyn}, and D_{FH} depend on the experimental setup and are optimized in our model. We adopt the following limiting values:

$$\begin{cases} 10^{-7} < D_{FH}\,[m] < 10^{-4} \\ 0 < \mu_s < 1 \\ 0 < \mu_{dyn} < 1 \end{cases} \tag{10}$$

and we start the optimization procedure with the initial guess values: $D_{FH} = 10^{-6}$ m, $\mu_s = 0.7$ and $\mu_{dyn} = 0.3$. Once the temperature on the sliding surface reaches the value for rock melting ($T \approx T_w$), a continuous layer of melt is formed separating the fault surfaces, and τ becomes a function of the melt viscosity η (Equation 3) (Nielsen, Di Toro, & Griffith, 2010; Nielsen et al., 2008). The melt viscosity η decreases with the average temperature on the slip surface T. Following (Giordano et al., 2008), we assume a Vogel-Fulcher-Tamman equation for the temperature dependent melt viscosity:

$$\log(\eta) = A + \frac{B}{T - C} \tag{11}$$

parameters A, B, and C are dependent on melt composition and experimental conditions (room humidity or pressurized fluids). The parameters A, B, C are estimated using the relationship proposed by Giordano et al. (2008) and the glass chemical composition for gabbro, Etna basalts and granitoid rocks (tonalite) reported in Violay et al. (2014, 2015) and Di Toro and Pennacchioni (2004), respectively. The parameters A, B, C used in the model are reported in Table S8 in Supporting Information S1.

The melt layer thickness $2w$ is a parameter affecting the dynamic response of the experimental fault during the weakening or breakdown stage (Equation 3). Its real value is probably higher than the one measured at the end of slip because of final and post-slip melt extrusion from the slip zone (Nielsen et al., 2008). Here we assume that melt thickness is also a function of the average temperature T and it can be computed by solving the Stefan problem of the advancement rate ν of the melting layer in the solid bulk rock (i.e., solving the heat diffusion inside the solid in presence of a moving boundary). To solve the problem, we use the same approach as in Nielsen, Di Toro, and Griffith (2010). For $z \leq w$ (into the melt layer thickness), the heat diffusion equation is:

$$\frac{\partial T}{\partial t} = \alpha_{th} \frac{\partial^2 T}{\partial \xi^2} + \nu \frac{\partial T}{\partial \xi} \tag{12}$$

where $\xi = z - w$ is the half thickness of the melt layer. The thickness of the melt layer w is defined as:

$$w = w_0 + \int \nu \, dt \tag{13}$$

with $\nu = \frac{w^3 \sigma_n}{K \eta R^2}$ where R is the sample radius, K is a geometrical factor taking into account the sample geometry and that can range from 0.02 for hollow cylinder samples with 30/50 mm internal/external diameter and $3/16 = 0.1875$ for solid cylinders (Nielsen et al., 2008). In our model we optimize K, to consider the possible change in sample area during shearing and melt formation. For $z > w$ (outside the melt layer thickness), the increase of temperature can be estimated as

$$\frac{\partial T}{\partial z} = \frac{1}{2} \tau V \frac{(T_m - T)}{\alpha_{th} \rho (L + C_p (T_m - T))} \tag{14}$$

with T_m the melting temperature and L the latent heat of melting. The contribution of L is neglected in this work.

3.2. Flash Heating and Dislocation Creep/Diffusion Model

For experiments performed on calcitic marble samples, the investigated weakening mechanism is a combination of flash heating and dislocation or diffusion creep (Equation 4, Table 1). For flash heating, the model is described in Section 3.1. The optimized parameters are μ_s, μ_{dyn}, and D_{FH}, with the limiting values reported in Equation 10 and the same initial guess values ($D_{FH} = 10^{-6}$ m, $\mu_s = 0.7$ and $\mu_{dyn} = 0.3$).

The pre-exponential factor is $A = 0.046$ s^{-1}bar^{-n} for dislocation creep and $A = 9.55 * 10^4$ s^{-1}bar^{-n} for diffusion creep (Schmid et al., 1987). The n value is obtained by inverting the experimental data (usually obtained in low velocity uniaxial experiments at high temperature) for a given activation energy value. Here we choose $H = 301.4$ kJ/mol and $H = 213.5$ kJ/mol for dislocation creep and diffusion creep, respectively (Schmid et al., 1977). With this activation energy $n = 5$, $b = 0$ for dislocation creep and $n = 1.7$, $b = 2$–3 for diffusion creep, respectively. In the presence of water, we impose a reduction of H of about 20% with $H = 238.6$ kJ/mol for dislocation creep and $H = 175.8$ kJ/mol for diffusion creep (see Rutter, 1972; Violay et al., 2019). Here, we decided to optimize also for n and b value respectively for the two mechanism in order to take into account the uncertainties that these parameters can assume at the extreme deformation condition of our experiments. For the dislocation creep model, the optimization procedure involves the parameter t (i.e., twice the layer thickness) with the limit values reported in Demurtas et al. (2019), De Paola et al. (2015), Pozzi et al. (2021):

$$\begin{cases} 3 < n < 7 \\ 10 < t \left[10^{-6}\text{m}\right] < 200 \end{cases} \tag{15}$$

The initial guess values are $n = 5$ and $t = 200\ 10^{-6}$ m.

For the diffusion creep model, the optimized parameters are the grain size D_D, the grain size exponent b, and the layer thickness t with the limit values as (Demurtas et al., 2019; De Paola et al., 2015; Pozzi et al., 2021):

$$\begin{cases} 10 < D_d \left[10^{-9}\ \text{m}\right] < 500 \\ 2 < b < 3 \\ 10 < t \left[10^{-6}\ \text{m}\right] < 200 \end{cases} \tag{16}$$

The initial guess values are $D_d = 200\ 10^{-9}$ m, $b = 2.5$ and $t = 200\ 10^{-6}$ m.

We can define the bulk shear stress τ as a function of the slip-switch distance (δ_0) such that:

$$\begin{cases} \tau = \tau_{FH} \text{ if } \delta < \delta_0 \\ \tau = \tau_D \quad \text{if } \delta \geq \delta_0 \end{cases} \tag{17}$$

4. Results

The weakening mechanisms described in the Introduction and analyzed in this study are listed in Table 1, together with the optimized parameters and the experimental conditions. The sets of optimized parameters for each experimental data are reported in Tables S1–S4 in Supporting Information S1. In the following, we will present the results of the optimization procedure in terms of mean and standard deviation values for the optimized parameters for each model (Table 2) and discuss the fit to the shear stress evolution as a function of slip resulting from the experiments. We emphasize that each model investigated in this study is discussed by analyzing a relatively large number of experimental data for various lithologies, which is not common in the literature.

4.1. Flash Heating and Bulk Melting Model

Flash heating and bulk melting weakening mechanisms are applied to experiments performed on silicate-built bare rocks including 13 experiments with basalt, 25 experiments with gabbro and 9 experiments with granitoid rocks. Values of the optimized parameters for each experiment are reported in Table S1 in Supporting Information S1.

Figure 3 shows the fit to shear stress evolution with slip for two experiments with basalt (S921) and gabbro (S609) using the optimized parameters. FH matches the initial part of the dynamic weakening curve up to a slip value of nearly 0.493 m for gabbro (Figure 3a) and 0.1 m for basalt (Figure 3b). At this low slip values bulk melting is not active because temperature has not yet reached the T_m. Flash heating alone does not explain both the subsequent stress breakdown and the stress level at the dynamic friction, yielding higher values of dynamic friction for both lithologies. The slip-switch distance (δ_0) is reached at mean slip values of 0.15 m for basalt and 0.5 m for gabbro, when the bulk melting weakening mechanism is activated. The latter matches both the stress level at the dynamic friction and the final restrengthening due to the imposed deceleration ramp. According to the composite model investigated in this study, there is the transition from flash heating to bulk melting when the latter yields the lowest values of the residuals, that is the lowest mismatch with experimental data. As expected, the imposed transition is too sharp, yielding a drop in shear stress evolution toward the dynamic friction level, not observed in experimental data (Figure 3). This suggests that there might likely be a range of slip values and temperatures for which both mechanisms work together, without a sudden transition. Nevertheless, the composite model yields average static and dynamic friction values that well match the shear stress evolution with slip.

For the flash heating and bulk melting model, the inferred average static friction coefficient is 0.99 ± 0.02, 0.88 ± 0.15, and 0.80 ± 0.10 for basalt, gabbro and granitoid rocks, respectively (Figure S4a in Supporting

Table 2
Summary of the Mean Values and Standard Deviation Values of the Optimized Parameters for Each Model as a Function of the Lithology

Flash heating and bulk melting

	μ_s		μ_{dyn}		D_{FH} [µm]		K_{hollow}		K_{fully}	
	Mean	Sdv	Mean	Sdv	Mean	Sdv	Mean	Sdv	Mean	Sdv
Basalt	0.99	0.02	0.21	0.17	15	7	0.0212	0.002	0.181	0.005
Gabbro	0.88	0.15	0.2	0.2	20	10	0.0212	0.002	0.181	0.005
Granitoid	0.8	0.1	0.3	0.13	70	20	0.0212	0.002	0.181	0.005

Flash heating and dislocation creep

	μ_s		μ_{dyn}		D_{FH} [µm]		n		t [µm]	
	Mean	Sdv	Mean	Sdv	Mean	Sdv	Mean	Sdv	Mean	Sdv
Calcitic marble	0.68	0.04	0.1	0.02	101	5	5	–	200	–

Flash heating and diffusion creep

	μ_s		μ_{dyn}		D_{FH} [µm]		D_D [nm]		b		t [µm]	
	Mean	Sdv	Mean	Sdv	Mean	Sdv	Mean	Sdv	Mean	Sdv	Mean	Sdv
Calcitic marble	0.67	0.05	0.1	0.05	100	50	90	20	2.97	0.03	199.4	0.3

Note. μ_s = static friction coefficient from the flash heating model optimization, μ_{dyn} = dynamic friction coefficient from the flash heating model optimization, D_{FH} = Asperity diameter from the flash heating model optimization, K_{hollow} and K_{fully} = geometrical factor, n = exponential factor, t = layer thickness, D_D = nanoparticles diameter, b = exponential factor

Information S1). The average dynamic friction coefficient is 0.21 ± 0.17, 0.20 ± 0.20, and 0.30 ± 0.13 for basalt, gabbro and granitoid rocks, respectively (Figure S4b in Supporting Information S1). The average D_{FH} is 15 ± 7, 20 ± 10, and 70 ± 20 µm for basalt, gabbro and granitoid rocks, respectively (Figure S4c in Supporting Information S1). D_{FH} is independent of the applied normal stress (Figure S4c in Supporting Information S1). The independency of D_{FH} from normal stress is an indication that a constant τ_c is a reliable assumption for the range of conditions investigated ($5 < \sigma_N < 40$ MPa). The geometrical factor K value is 0.0212 ± 0.002 for hollow

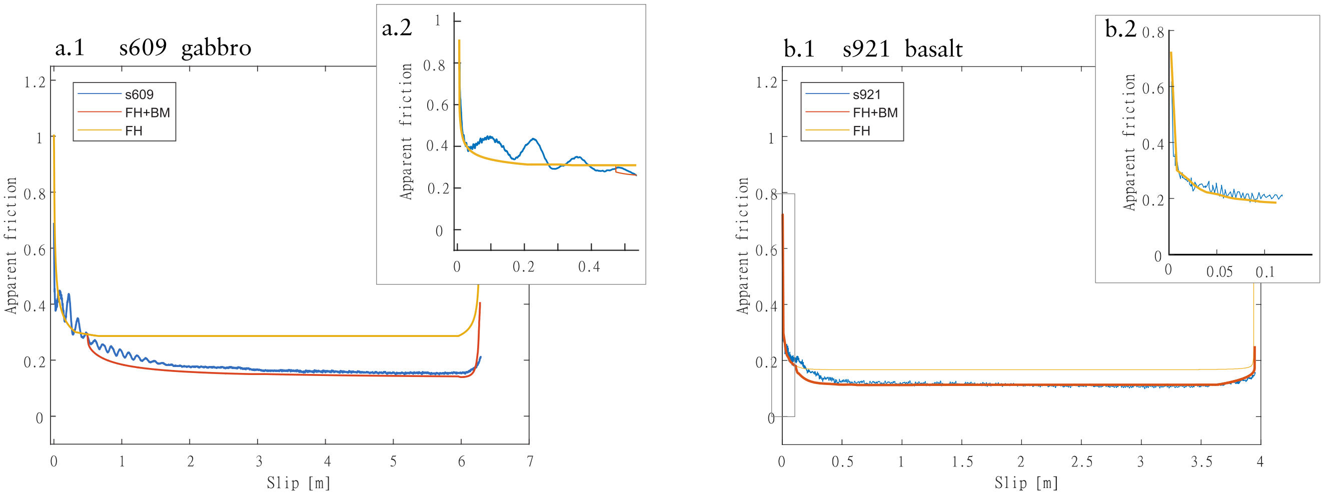

Figure 3. Flash heating and bulk melting composite model optimization. Examples of optimization of flash heating and bulk melting model for (a) experiment s609 performed on gabbro at 10 MPa normal stress under room humidity condition and target slip-rate $V_t = 2$ m/s and (b) experiment s921 performed on basalt at 25 MPa total normal stress, 5.7 fluid pressure and target slip-rate $V_t = 3$ m/s. The flash heating mechanism (yellow curve) was well representative of our experimental data until slip reached $\delta_0 = 0.493$ and 0.101 m, respectively. After this slip distances, bulk melting lubrication mechanism was activated with the modeled temperature higher than the melting one ($T > T_m$). The resulting curve of optimization (orange curve) was obtained with $\mu_s = 0.98$, $\mu_{dyn} = 0.20$ and $D_{FH} = 5$ µm for experiment s609 and $\mu_s = 1$, $\mu_{dyn} = 0.1$ and $D_{FH} = 19$ µm for experiment s921.

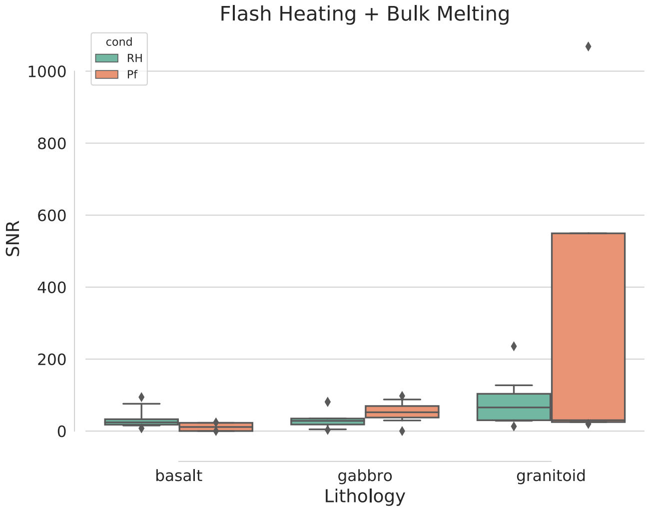

Figure 4. Boxplots for the squared norm value of the residuals (SNR) of the flash heating and bulk melting model as a function of the sample lithology (basalt, gabbro, granitoid rocks) and the experimental condition (room humidity or fluid pressurized. The SNR is a measure of the goodness of the fit of the experimental curve by the proposed model, the lower the SNR, the better the fit of the experimental curve was. The median lower SNR was for basalt rocks experiments, while the higher SNR was for granitoid rocks experiments.

cylinder samples and 0.181 ± 0.005 for fully cylinder samples and very close to the theoretical expected one (0.02 and 0.1875 for hollow cylinder and fully cylinder, respectively, (Nielsen et al., 2008)) (Figure S5 in Supporting Information S1).

The inferred SNR values obtained with the composite model and associated with the optimized parameters for silicate-built bare rocks are shown in Figure 4. The distribution of the median SNR values for the different lithologies is quite narrow, with mean values ranging between 27.6 and 147.8, for basalt and granitoid rocks, respectively. In the boxplots, the distribution of SNR values is narrow except for the granitoid rocks, in particular those sheared in presence of pressurized fluids. The distributions of SNR values for basalt and gabbro are slightly asymmetric with more values toward the minimum, while SNR values for the granitoid sheared in presence of pressurized fluids are spread over a large interval asymmetric toward the maximum. The boxplots analysis allows the identification of a few outliers (diamonds in Figure 4). The worst performance of the granitoid rocks is determined by the shear stress evolution at the dynamic friction which, unlike the other lithologies, shows an increase before achieving the dynamic friction value (Hung et al., 2019).

4.2. Flash Heating and Dislocation Creep Model

The flash heating and dislocation creep weakening mechanisms are applied to 50 experiments performed with calcitic marble. Values of the optimized parameters for each experiment are reported in Table S2 in Supporting Information S1, while Table 2 shows mean and standard deviation values. The optimized parameters for diffusion creep are n and t (Equation 4).

For the flash heating, the average value is 0.68 ± 0.04, 0.10 ± 0.02 and 101 ± 5 μm for static friction, dynamic friction and asperity size, respectively. According to this model, in all the experiments, dislocation creep is not activated and the values of n and t remain equal to the initial guess values ($n = 5$ and $t = 200$ μm) (Figure 5a) and the match with experimental data is poor as corroborated by the retrieved high SNR values (Figure 6a). On average, the SNR value is 98.69 for experiments performed under room humidity conditions and 261.68 for experiments performed with pressurized fluids.

4.3. Flash Heating and Diffusion Creep Model

The flash heating and diffusion creep model is applied to 50 experiments performed with calcitic marble. Values of the optimized parameters for each experiment are reported in Table S3 in Supporting Information S1, while Table 2 shows mean and standard deviation values. For the first phase of flash heating, the average value is 0.67 ± 0.05, 0.10 ± 0.05 and 100 ± 50 μm for static friction, dynamic friction and asperity size, respectively (Figure S4 in Supporting Information S1). The optimized parameters for diffusion creep are D_D, b and t (Equation 4). The average values obtained through the optimization procedure are 90 ± 20 nm for the grain size D_D, 2.97 ± 0.03 for the grain size exponent b, and 199.4 ± 0.3 μm for the layer thickness t (Figure S4 in Supporting Information S1). The average values modeled for diffusion creep agree with values used by several authors (De Paola et al., 2015; Harbord et al., 2021; Schmid et al., 1977) for high velocity experiments, while the optimized layer thickness is slightly higher compared to Harbord et al. (2021) (100 μm) and De Paola et al. (2015) (150 μm).

Figure 5d shows the fit to shear stress evolution with slip for an experiment with calcitic marble (S1684) sheared at room conditions using the optimized parameters. As in the case of bulk melting, FH matches the initial part of the dynamic weakening curve quite well, but it does not match the shear stress at the dynamic friction level. Instead, diffusion creep is activated at a slip distance of 0.28 m, and it matches very well the stress at the dynamic friction. For this model the slip-switch distance δ_0 between flash heating and diffusion creep is normal stress dependent (Figure 8b), decreasing from ~0.39 m at $\sigma_n \leq 10$ MPa to 0.07 m at $\sigma_n > 20$ MPa. In average, the SNR

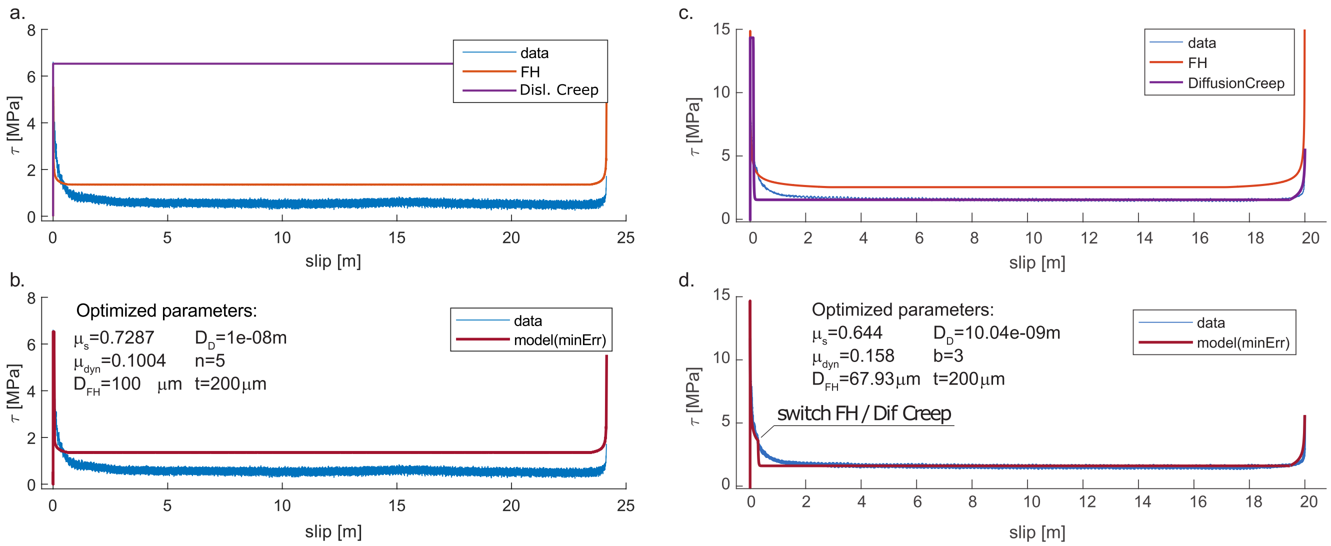

Figure 5. Flash heating and dislocation creep composite model and Flash heating and diffusion creep composite model. (a and b) Example of flash heating and dislocation creep model optimized for experiment s330, performed on calcitic marble sample under room humidity condition (RH), 10 MPa normal stress and target slip-rate $V_t = 3$ m/s. The dislocation creep mechanism (purple curve) was not able to represent the decrease of shear stress with slip. Consequently, the final shear stress model (b), red curve) was only given by the flash heating mechanisms (a) orange curve). (c and d) Example of flash heating and diffusion creep model optimized for experiment s1684 (blue curve), performed on calcitic marble sample sheared under RHs, 20 MPa normal stress and $V_t = 6$ m/s. According to our modeling results, the flash heating mechanism (orange curve) was active during the first stage of slip until a slip distance $\delta_0 = 0.280$ m. After this slip distance, the diffusion creep mechanism (purple curve) approximates better our experimental results (blue curve). The red curve represented the composed modeled shear stress evolution.

value is 0.008 for experiments performed under room humidity conditions and 0.005 for experiments performed in the presence of pressurized fluids (Figure 6b).

For all lithologies, the flash heating models show that the average asperities dimensions D_{FH} (Table 2), inferred in this study through the composite models, are similar to those previously proposed for basalt and gabbro (Passelègue et al., 2014; Rempel & Weaver, 2008), but twice the value of the asperity dimensions measured before the experiment for calcitic marble and granitoid rocks (Cornelio et al., 2019, 2020) (Figure S4c in Supporting Information S1).

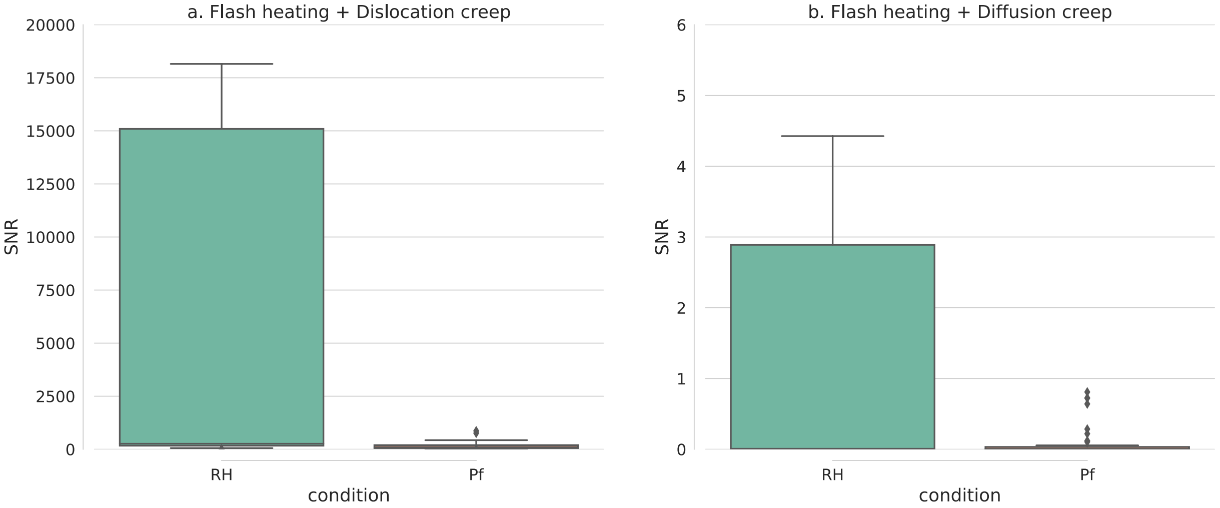

Figure 6. Boxplots of the squared norm value of the residuals (SNR) for (a) flash heating and dislocation creep model and for (b) flash heating and diffusion creep model for experiments performed on calcitic marble rocks. The SNR is a measure of the goodness of the fit of the experimental curve by the proposed model, the lower the SNR, the better the fit of the experimental curve was. Comparing the values of the SNR we can observe that it was lower for the flash heating and diffusion creep model (median values of 0.0078 and 0.0047, for room humidity and fluid pressurized experiments, respectively) than the one for flash heating and dislocation creep model (median values of 256.0 and 98.7, for room humidity and fluid pressurized experiments, respectively).

5. Discussion

Our modeling results corroborate previous findings (Beeler et al., 2008; Goldsby & Tullis, 2011) that flash heating provides a good fit to the shear stress evolution with slip around the peak stress, when apparent friction is at its static value, and at the incipient stage of weakening for all the lithologies and composite models investigated in this study. The adopted optimization procedure indicates that the values of modeled static friction coefficient for all lithologies are in agreement with Byerlee's friction law (Byerlee, 1978) at these applied effective normal stresses ($\sigma'_n = 5$–40 MPa) and range from 0.67 for calcitic marble to 0.99 for basalt (Table 2), without an evident dependency on normal stress (Figure S4a in Supporting Information S1). Moreover, our modeling results show that flash heating alone does not explain the subsequent weakening to the dynamic friction level, yielding higher predicted values of dynamic friction for all lithologies. This observation supports the hypothesis that other dynamic weakening mechanisms are necessary to reproduce the inferred stress evolution at the dynamic friction level for experiments performed at these high sliding velocities (Nielsen et al., 2021). Depending on the lithology, melting for silicate-built rocks and diffusion creep for calcitic marble seem to be the most efficient mechanisms, among those here investigated, to explain the measured values of dynamic friction. The optimized dynamic friction coefficient (Figure S4b in Supporting Information S1) inferred with the composite models ranges between 0.1 for calcitic marble and 0.3 for granitoid rocks, in agreement with values from literature (Goldsby & Tullis, 2011; Passelègue et al., 2014; Rice, 2006).

Shear stress evolution with slip inferred from experiments performed on silicate-built bare rocks, such as basalt and gabbro, is relatively well reproduced by the composite model made of flash heating and bulk melting, except of granitoid rocks for which the model yields the highest SNR values at low effective normal stress (≤10 MPa) (Figure S7 in Supporting Information S1). A possible explanation is that our viscosity model does not include the complexity of selective melting typical of frictional melting in granitoid rocks (Di Toro & Pennacchioni, 2004; Hung et al., 2019; Papa et al., 2021). Indeed, dedicated high-velocity experiments using granitoid rocks showed that at low normal stresses (≤10 MPa) the compositional and structural evolution of the melt layer is extremely complex (Hung et al., 2019). Granitoid rocks are made of minerals with low and high melting points (e.g., biotite 650°C, feldspar 1100–1200°C, quartz 1700°C (Spray, 2010)). Because of this, the first discontinuous melt patches are ultramafic in composition (biotite melts first) but have a low temperature and are rich in quartz and feldspar clasts (Hung et al., 2019). Moreover, the friction melt-wall rock boundary is very rough at these low frictional dissipation rates (Nielsen, Di Toro, & Griffith, 2010). These compositional and geometrical properties affect the viscosity and the bulk rheology of the sheared friction melt layer and are not included in our model. On the contrary, the SNR value is lower (Figure 4) for rock types where frictional melting involves minerals with relatively similar melting points as in the case of basalt and gabbro (feldspar 1100–1200°C, amphiboles 1100–1200°C, pyroxene 1400°C, (Spray, 2010)). These considerations confirm that, not only different dynamic weakening mechanisms coexist and are necessary to model shear stress evolution with slip at high slip-rates, but the lithology and the evolution of thermal properties (and viscosity in case of melts) with slip does also matter in determining the frictional response of the experimental fault when shared at high slip-rates.

Our modeling attempts of experiments performed with calcitic marble suggest that the flash heating and diffusion creep composite model matches better the shear stress evolution with slip than the flash heating and dislocation creep model as shown by the inferred SNR values (Figure 6). The obtained values of the optimized parameter D_D and b for diffusion creep are in agreement with the experimental results from literature (Schmid et al., 1977). Also for this lithology, the flash heating model alone is not suitable to represent the shear stress decrease and evolution at the dynamic friction level in agreement with previous works (Demurtas et al., 2019; Pozzi et al., 2019). The high SNR values inferred for dislocation creep suggest that at these high slip values the processes responsible for this mechanism are not active or that they are not representative of the stress evolution with progressive slip at the dynamic friction. Under the investigated experimental conditions, the grain size dependency of grain boundary sliding aided by diffusion creep make this process more efficient than dislocation creep within the PSZ. To test the validity of the proposed optimization procedure with the composite model, we tested the FH and diffusion creep composed model on experiments performed on gabbro (Figures S2a and S2b in Supporting Information S1) and basalt (Figures S2c and S2d in Supporting Information S1). We consider this test as a reductio ad absurdum because several microstructural and theoretical evidence (Hirose & Shimamoto, 2005; Nielsen et al., 2008) suggest that bulk melting, rather than diffusion creep, is controlling the frictional strength of gabbro at the steady-state dynamic friction. Our results confirm that FH and diffusion creep are not efficient to match the

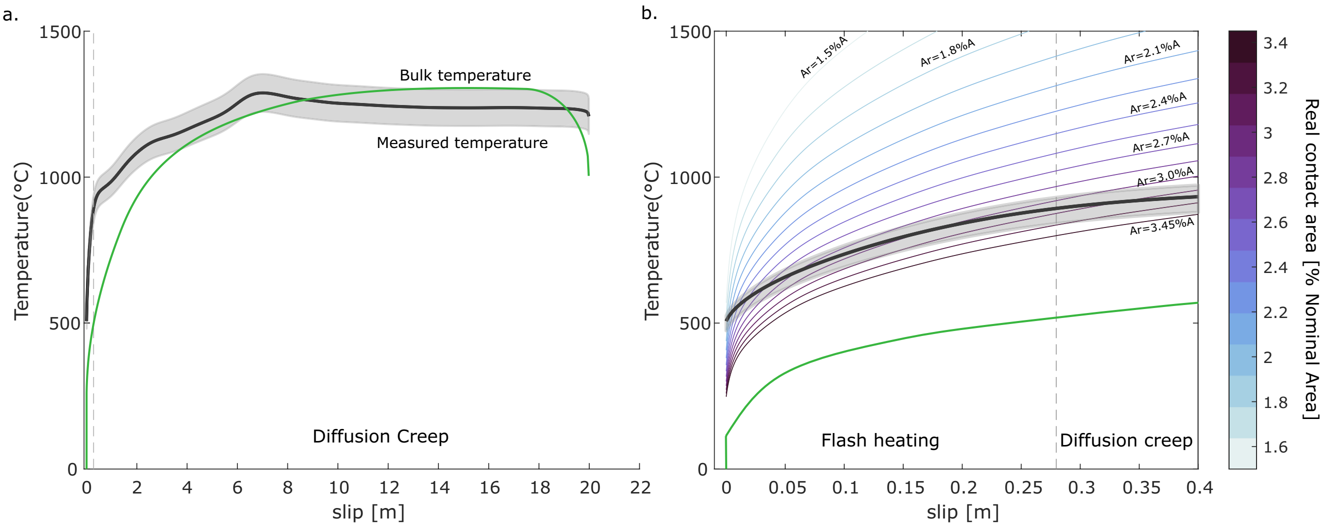

Figure 7. Temperature evolution for experiment s1684: measured temperature with optical fibers (black line, Aretusini, Núñez-Cascajero, et al., 2021) compared with the estimated temperature for flash heating and diffusion creep model (green line). For the flash temperature, various percentages of the real contact area were taken into consideration. (a) Measured temperature (black line) with 5% error on the measurements (gray area) (Aretusini, Núñez-Cascajero, et al., 2021) for the entire experiments compared with the diffusion bulk temperature used for the diffusion creep model only (green line). (b) Zoom on the first 0.4 m of slip. Considering a constant diameter of the asperity $D_{FH} = 63$ μm (independent of slip distance, see main text), the measured temperature suggest an increase of the real contact area from 1.5% of the nominal area to 3.15% for slip distance equal to δ_0 (gray dashed vertical line).

shear stress evolution with slip of gabbro and basalt, where FH and bulk melting are effective. This confirms that the increase of temperature in the slip zone caused by flash heating activates different weakening mechanisms at high slip-rates depending on the lithology and normal stress conditions.

It is well known that temperature has a pivotal role in controlling the coseismic shear stress by activating dynamic weakening processes as pointed out in the literature (Di Toro et al., 2011; Nielsen et al., 2021) and further corroborated by our results. However, most of the studies use numerically computed values of expected temperature of the slip zone (see Methods). Temperatures measurements at high slip-rates are technically challenging because of the thermal inertia of thermocouples and their poor spatial and temporal resolution. In this work we avail of recent in-situ temperature measurements performed with a novel technology which uses optical fibers (Aretusini, Núñez-Cascajero, et al., 2021; Nunez Cascajero et al., 2021). For the first time, we use the high spatial resolution (investigated diameter ~40 μm) and high sampling rates (sampling time 0.001 s) of temperature measurements to calibrate the numerical model of temperature increase in the slip zone. Experiment s1684 (see Figure 7) has been performed at a slip-rate of 6 m/s and 20 MPa normal stress under room humidity conditions in calcitic marble samples (30/50 mm internal/external diameter). We applied the optimization procedure using the composed model of the flash heating and diffusion creep which yields $\mu_s = 0.64$, $\mu_{dyn} = 0.16$ and $D_{FH} = 70$ μm for the flash heating mechanism, and $D_D = 10$ nm, $t = 200$ μm and $b = 3$ for the diffusion creep mechanism (Figure 5). For this experiment, we have compared the measured temperature in the slip zone with the value estimated from the diffusion creep model (Figure 7). The comparison (Figure 7a) shows that the two estimates agree within a 5% of error for slip values larger than 3 m. For the first centimeters of slip (Figure 7b), until the slip-switch distance $\delta_0 = 0.280$ m, we can estimate the flash temperature T_{flash} (Archard, 1958; Rice, 2006) as follows:

$$T_{flash} = \frac{1}{\rho C_p \sqrt{(\alpha_{th}\pi)}} \tau_c V \sqrt{(t_c)} \tag{18}$$

with $\alpha_{th} = 1.4$ m$^2/s$ thermal diffusivity of the calcitic marble, ρC_p specific heat (Table S3 in Supporting Information S1), τ_c critical contact shear stress ($\tau_c = \frac{\tau_p}{A_r}$ where A_r is the real contact area) for a single crystalline asperity and t_c the sliding lifetime of an asperity. The real contact area A_r is the unknown in Equation 18 and it is a small percentage (usually around 5%, (Dieterich & Kilgore, 1994; Persson, 2006) of the nominal area $A = \pi(r_e{}^2 - r_i{}^2)$, where $r_e = 0.025$ m and $r_i = 0.015$ m are the external and internal radius, respectively, of the hollow rock cylinder used in the experiment. The lifetime of the asperity is $t_c = \frac{D_{FH}}{V}$ assuming an average asperity dimension equal to

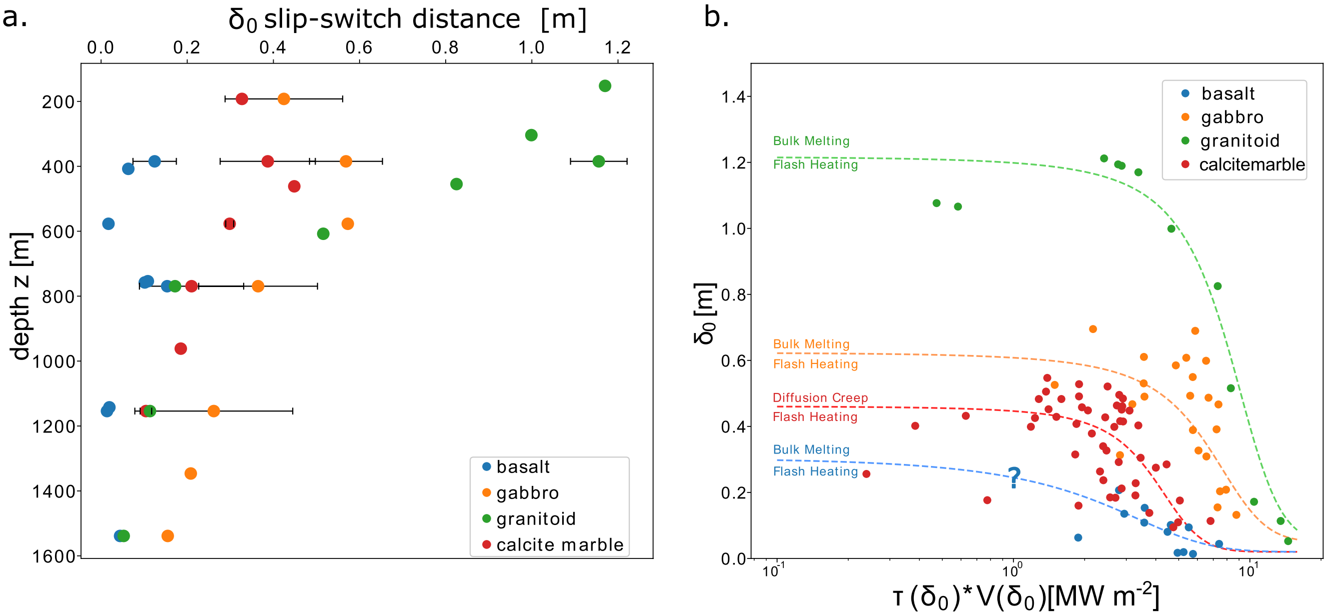

Figure 8. Evolution of slip-switch distance vs. (a) depth z and (b) instantaneous power (PD). (a) Considering a linear relation between the normal stress applied in our experiment and the depth z, we observe the decrease of the slip-switch distance with depth. (b) With increasing instantaneous PD, the slip-switch distance decrease for all rock types. For visualization purposes, the points in this slip-switch distance versus PD diagram were interpolated by four dashed lines defined by a sigmoidal function $y = a\left(1 - \frac{1}{1+\exp(-b*(x-c))}\right)$. Below each dashed line (colors represent different rock types and combinations of weakening mechanisms), asperity-scale mechanisms (i.e., flash heating) govern dynamic fault weakening; above each dashed line, bulk weakening mechanisms (bulk melting or diffusion creep) govern the dynamic fault weakening.

the optimized value D_{FH}, and the slip-rate V variable in time and equal to the imposed one. Considering A_r as the unknown, in Figure 7b we report the modeled T_{flash} for increasing percentages of A_r. The temperature measured in the slip zone with the optical fiber is well approximated by a modeled T_{flash} for an initial real contact area of ca. 1.5% which increases to 3.15% of the nominal area A at the slip-switch distance δ_0 of 0.280 m (Figure 7b).

At the slip-switch value, when the diffusion creep model becomes the most representative controlling the shear stress evolution, the measured temperature is larger than the estimated temperature. This difference (ca. 500 K) might suggest changes in thermal properties, not included in the FH model used in this study. In other words, for slip values up to the slip-switch distance, when flash heating is assumed to control the shear stress evolution, the measured temperature and the heat source are much larger than the modeled values. Nevertheless, FH is able to match quite well the evolution of shear stresses with slip. The difference between modeled and measured temperatures is largest for slip values between the slip-switch and the slip required to reach the dynamic friction value. In this slip interval the composed model is also underperforming to reproduce the measured shear stress. This slip interval correspond to the range in which diffusion creep does not match well the shear stress evolution curve due to the sharp transition to the dynamic friction. This implies that the temperature used in the composite model underestimates the real temperature measured in the sample. At slip distances larger than 3 m, the composed model reproduces the shear stress evolution and the dynamic friction level, and the estimated and measured temperatures agree (i.e., within the errors with a model of diffusion creep). For slip smaller than the slip-switch distance, the composed model fit the shear stress and the estimated temperature is in good agreement with the measured one, under the hypothesis that the real area of contact is a small percentage of the nominal one. These results suggest that the temperature necessary to activate diffusion creep can be reached even earlier and at lower slip distances than those predicted by the composite model, because either thermal (C_p, ρ) or mechanical (D_{FH}) parameters are varying during the dynamic weakening or breakdown stage or because other mechanisms (e.g., decarbonation) might be activated. Moreover, because we deal with bare surfaces samples, we considered, in our model, a constant PSZ thickness. However, previous studies revealed that compaction, pressure solution and slip localization play a pivotal role in controlling the evolution of shear stress, especially if the sample is made of a gouge layer (X. Chen et al., 2021; Pozzi et al., 2018; Smith et al., 2015).

Finally, to quantify the goodness of the modeled temperature compared with the measured one, we used the regression coefficient as $R^2 = \frac{\Sigma\left(T_{meas,i} - T_{mod,i}\right)^2}{\Sigma\left(T_{mod,i} - \overline{T}\right)^2}$ =0.7 with $\overline{T}$ average value of the measurements of temperature. By definition, as R^2 approaches 1, the measurements of temperature are more consistent with those obtained in the model and with the estimate of the slip-switch distance between the two considered dynamic weakening mechanisms. Our values of $R^2 = 0.7$ show a general good agreement between modeled and measured values.

Within the uncertainties of temperature measurements and model simplifications, it is possible to speculate that multiple dynamic weakening models coexist during the weakening stage and that the transition from flash heating to other thermally activated processes is not sharp, rather it occurs over a slip range in which temperature further increases and friction continues to decrease to its dynamic level. The shear stress evolution with slip during the transition stage from the FH to other dynamic weakening mechanisms depends on the composed effects of different competing processes. Temperature is confirmed to be the controlling parameter causing the activation and the mutual interaction among processes occurring during the weakening stage at high slip-rates. However, determining the effective bulk temperature during sliding at high slip-rates is challenging but necessary to interpret shear stress evolution.

In this study, we have inferred the slip-switch value to identify the range of slip values in which flash heating is governing the shear stress evolution with slip as well as the slip values in which the bulk weakening mechanisms are expected to be activated to control shear stress. We remember that the slip-switch distance is a function of the adopted physical parameters (Table S7 in Supporting Information S1), since only after reaching T_w, the bulk weakening mechanism can be activated and rock properties as thermal conductivity, rock density and specific heat capacity, influence the shear stress reduction.

Based on the analysis of the experimental data set presented in this study for a limited set of lithologies (cohesive silicate-built and carbonate-built rocks) and using only bare surface samples, the slip distance for the switch between flash heating and bulk melting or diffusion creep mechanisms decreases with the increasing effective normal stress (i.e., depth) on the experimental fault (Figure S7 in Supporting Information S1 and Figure 8). In particular, the basalt at $\sigma'_n > 30$ MPa has the lowest slip-switch distance ($\delta_0 \sim 0.1$ m), while the granitoid rocks at $\sigma'_n < 10$ MPa have the highest slip-switch distance ($\delta_0 \sim 1.2$ m). Moreover, considering a linear relationship between effective normal stress and depth z ($\sigma'_n = \rho\ g\ z$, with $g = 9.81$ m/s^2 gravitational acceleration), the slip-switch distance decrease to few centimeters at 2 km depth (Figure 8a). For FH model, the slip-switch distance δ_0 identifying the transition between flash heating and a bulk process is lithology and normal stress dependent (Figure 8a), and spans from ∼0.03 m for basalt sheared at $\sigma_n > 20$ MPa to ∼1.2 m for granitoid sheared at $\sigma_\mathrm{n} \leq 10$ MPa.

The instantaneous PD at slip-switch distance was computed as:

$$PD = \tau\,(\delta_0)\ V\,(\delta_0) \tag{19}$$

with $\tau(\delta_0)$ the measured shear stress and $V\,(\delta_0)$ the measured slip-rate at slip-switch δ_0 in the analyzed experiments. Previous studies showed how the *PD* can be correlated to the dissipation of frictional heat during seismic slip and be used to describe the activation of seismic slip dynamic weakening mechanisms (Di Toro et al., 2011). The *PD* also affects the frictional work comprising frictional heat (Tinti et al., 2005). Moreover, the *PD* and the frictional work associated with experimental deformation at seismic slip-rates is comparable to the one dissipated during natural earthquakes (Di Toro et al., 2011; Nielsen et al., 2016). Our compilation of *PD* shows an inverse dependence with slip-switch distance (Figure 8b) which resembles the inverse dependence of *PD* with slip weakening distance in Di Toro et al. (2011). This dependence implies a direct dependence of slip-switch distance with slip-rate function *V* and an inverse dependence of slip-switch distance with normal stress (Figure S7 in Supporting Information S1). In other words, with increasing *PD*, the higher frictional power dissipation (either because of higher slip-rates at constant normal stress or by higher normal stress with constant slip-rates) activates the bulk weakening processes at lower slip-switch distances. By means of our relation between slip-switch distance and *PD* (Figure 8b), it can be estimated that at seismogenic depths (9–12 km depth, possibly corresponding to 150–200 MPa normal stress on the fault) and seismic slip-rates of ca. 1 m/s, the slip-switch distance shrinks to few centimeters or millimeters.

Moreover, considering that the earthquake magnitude increases with fault average slip, it raises the question of the role of flash heating in small earthquakes when the slip switch distance is less than the average slip of the seismic event (Figure S8 in Supporting Information S1). We speculate that in these conditions flash heating and weakening might be significant for small magnitude earthquakes. This suggests that, according to the laboratory results, dynamic fault weakening during small magnitude earthquakes might be modeled only with flash heating without considering other competing processes, if natural fault zones can be represented by the bare surfaces approximation adopted at the laboratory scale. Our observations seem also to suggest that for large magnitude earthquakes a composed model is necessary to explain dynamic fault weakening at large slip values and account for the transition to bulk slip zones processes. However, we emphasize that natural faults present a more complex geometry and composition compared to our experimental set-up and direct extrapolation to natural cases is not travial. Indeed, slip zones in natural faults can be often structured as more or less continuous and cohesive surfaces sandwiching mm-cm thick, fluid-rich, gouge layers (e.g., Demurtas et al., 2016; Masoch et al., 2019). The presence of gouges may lead to more distributed deformation, alternating episodes of localization and delocalization, which may buffer the weakening effects of flash heating under similar seismic condition. In our composite model, a more gradual transition between weakening models can be achieved by considering the total strain rate as the sum of the strain rates accommodated by each mechanism. In this case, the most effective mechanism is expected to yield the highest strain rate, therefore governing the stress-strain relation during the dynamic weakening stage. However, formulating a constitutive relation in terms of strain and strain rate opens the question of the scale dependence of constitutive processes, which is beyond the goal of the present study. Moreover, only slip-rate can be measured directly while the shear strain rate suffers from uncertainties in the estimation the finite width of the slip zone. The dependence of constitutive laws on strain and strain rates has been already proposed in the literature (Beeler et al., 1996, among several others), but its application to interpret experimental data collected in laboratory experiments is still a challenge to tackle in future investigations.

6. Conclusions

Rock friction experiments conducted in the last 25 years to reproduce seismic slip deformation conditions for bare surfaces highlighted that dynamic fault weakening is associated with the activation of multiple asperity- (tens of micrometers) and PSZ-scale (mm to cm) deformation mechanisms. Here we discuss the dynamic weakening mechanisms that best describe the experimental evidence and the transition from one mechanism (asperity scale, i.e., flash heating and weakening) to another (PSZ-scale, i.e., bulk melting, dislocation creep and diffusion creep) with increasing coseismic slip. To achieve this goal, we analyze almost 100 high velocity friction experiments performed on bare rock samples of basalt, gabbro, granitoids (Westerly granite and tonalite) and calcitic marbles, at 5–40 MPa effective normal stress, under room humidity to fluid pressurized conditions. We used an optimization procedure to determine values of parameters that describe the weakening mechanisms. We fit the measured shear stress evolution with slip using a composed weakening model, which, depending on lithology, include: (a) flash heating and bulk melting (granitoid, gabbro and basalt), (b) flash heating and diffusion creep (calcitic marble), (c) flash heating and dislocation creep (calcitic marble). We provide a set of optimized parameters, which are specific for each mechanism. These optimized parameters were obtained by minimizing the misfit between experimental data and model, namely, by solving a nonlinear least-squares curve fitting problem using the trust-region-reflective algorithm. This analysis allowed us to evaluate the suitability of the composed dynamic weakening models (Figures 3–5, S2, and S3 in Supporting Information S1). In particular, our results show that:

1. For silicate-built rocks, in gabbro and basalt, dynamic weakening is well described by the transition from flash heating to bulk melt lubrication. However, the SNR value increases (i.e., the model does not fit well the mechanical data) with increasing melt “complexity” (i.e., in granitoid rocks).
2. For calcitic marble, dynamic weakening is well described by the transition from flash heating to diffusion creep. In fact, the SNR value is lower (i.e., the model fits well the experimental data) than for the case of the transition from flash heating to dislocation creep model.

Moreover, the proposed modeling procedure allow us to retrieve the slip-switch distance δ_0, that is, the slip necessary for the complete transition from the asperity-scale to PSZ scale dynamic weakening mechanism (Figure 8). Our analysis shows that the δ_0 decreases with increasing effective normal stress acting on the fault (Figure S7 in Supporting Information S1), and it is a function of rock composition and slip-rate. This study provides constitutive parameters and their uncertainties together with their range of variability to be included in physically- and geologically-based dynamic earthquake simulations.

Data Availability Statement

All raw experimental data are available at https://doi.org/10.5281/zenodo.6341640.

Acknowledgments

This study has received funding from the European Research Council (ERC) under the European Union's Horizon 2020 research and innovation programme (grant agreement No 856559). MC participated in this work as Principal Investigator of the European Research Council (ERC) project FEAR (grant 856559) under the European Community's Horizon 2020 Framework Programme. SA participated in this work in the framework of the European Research Council (ERC) project FEAR (grant 856559) under the European Community's Horizon 2020 Framework Programme. This work was partially supported by Project MIUR 2020–2029 Working Earth – "Working Earth: Geosciences and understanding of the earth dynamics and natural hazards". We acknowledge the ERC Consolidator Grant 614705 NOFEAR. C.C. acknowledge A. Cornelio for suggestions on improving the optimization procedure. Authors acknowledge J. Chen and J. Bedford, for their comments to the paper. Open Access Funding provided by Istituto Nazionale di Geofisica e Vulcanologia within the CRUI–CARE Agreement.

References

Acosta, M., Passelègue, F. X., Schubnel, A., & Violay, M. (2018). Dynamic weakening during earthquakes controlled by fluid thermodynamics. *Nature Communications*, *9*(1), 3074. https://doi.org/10.1038/s41467-018-05603-9

Andrews, D. J. (2002). A fault constitutive relation accounting for thermal pressurization of pore fluid. *Journal of Geophysical Research*, *107*(B12), ESE 15-1–ESE 15-8. https://doi.org/10.1029/2002JB001942

Archard, J. F. (1958). The temperature of rubbing surfaces. *Wear*, *2*(59), 438–455. https://doi.org/10.1016/0043-1648(59)90159-0

Aretusini, S., Meneghini, F., Spagnuolo, E., Harbord, C. W., & Di Toro, G. (2021). Fluid pressurisation and earthquake propagation in the Hikurangi subduction zone. *Nature Communications*, *12*(1), 2481. https://doi.org/10.1038/s41467-021-22805-w

Aretusini, S., Mittempergher, S., Plümper, O., Spagnuolo, E., Gualtieri, A. F., & Di Toro, G. (2017). Production of nanoparticles during experimental deformation of smectite and implications for seismic slip. *Earth and Planetary Science Letters*, *463*, 221–231. https://doi.org/10.1016/j.epsl.2017.01.048

Aretusini, S., Núñez-Cascajero, A., Spagnuolo, E., Tapetado, A., Vázquez, C., & Di Toro, G. (2021). Fast and localized temperature measurements during simulated earthquakes in carbonate rocks. *Geophysical Research Letters*, *48*(9), e2020GL091856. https://doi.org/10.1029/2020GL091856

Aretusini, S., Spagnuolo, E., Dalconi, M. C., Di Toro, G., & Rutter, E. H. (2019). Water availability and deformation processes in smectite-rich gouges during seismic slip. *Journal of Geophysical Research: Solid Earth*, *124*(11), 10855–10876. https://doi.org/10.1029/2019JB018229

Austrheim, H., & Boundy, T. M. (1994). Pseudotachylytes generated during seismic faulting and eclogitization of the deep crust. *Science*, *265*(5168), 82–83. https://doi.org/10.1126/science.265.5168.82

Beeler, N. M., Tullis, T. E., Blanpied, M. L., & Weeks, J. D. (1996). Frictional behavior of large displacement experimental faults. *Journal of Geophysical Research B: Solid Earth*, *101*(4), 8697–8715. https://doi.org/10.1029/96jb00411

Beeler, N. M., Tullis, T. E., & Goldsby, D. L. (2008). Constitutive relationships and physical basis of fault strength due to flash heating. *Journal of Geophysical Research*, *113*(B1), B01401. https://doi.org/10.1029/2007JB004988

Boullier, A.-M., Ohtani, T., Fujimoto, K., Ito, H., & Dubois, M. (2001). Fluid inclusions in pseudotachylytes from the Nojima fault, Japan. *Journal of Geophysical Research*, *106*(B10), 21965–21977. https://doi.org/10.1029/2000JB000043

Brantut, N., & Platt, J. D. (2017). Dynamic weakening and the depth dependence of earthquake faulting (pp. 171–194). https://doi.org/10.1002/9781119156895.ch9

Brantut, N., Schubnel, A., Corvisier, J., & Sarout, J. (2010). Thermochemical pressurization of faults during coseismic slip. *Journal of Geophysical Research*, *115*(5), 1–17. https://doi.org/10.1029/2009JB006533

Brantut, N., Schubnel, A., Rouzaud, J.-N., Brunet, F., & Shimamoto, T. (2008). High-velocity frictional properties of a clay-bearing fault gouge and implications for earthquake mechanics. *Journal of Geophysical Research*, *113*(B10), B10401. https://doi.org/10.1029/2007JB005551

Brodsky, E. E., & Kanamori, H. (2001). Elastohydrodynamic lubrication of faults. *Journal of Geophysical Research*, *106*(B8), 16357–16374. https://doi.org/10.1029/2001JB000430

Byerlee, J. (1978). Friction of rocks. *Pure and Applied Geophysics PAGEOPH*, *116*(4–5), 615–626. https://doi.org/10.1007/BF00876528

Caine, J. S., Evans, J. P., & Forster, C. B. (1996). Fault zone architecture and permeability structure. *Geology*, *24*(11), 1025. https://doi.org/10.1130/0091-7613(1996)024<1025:FZAAPS>2.3.CO;2

Carslaw, H. S., & Jaeger, J. C. (1959). *Conduction of Heat in solids*(2nd Edn). Oxford University Press.

Castagna, A. (2012). Stima della potenza dissipata per attrito durante i terremoti: Confronto tra faglie sperimentali e naturali.= estimate of frictional seismic power dissipation from natural and experimental faults.

Chen, J., Niemeijer, A. R., & Fokker, P. A. (2017). Vaporization of fault water during seismic slip. *Journal of Geophysical Research: Solid Earth*, *122*(6), 4237–4276. https://doi.org/10.1002/2016JB013824

Chen, X., Chitta, S. S., Zu, X., & Reches, Z. (2021). Dynamic fault weakening during earthquakes: Rupture or friction? *Earth and Planetary Science Letters*, *575*, 117165. https://doi.org/10.1016/j.epsl.2021.117165

Chester, F. M., & Chester, J. S. (1998). Ultracataclasite structure and friction processes of the Punchbowl fault, San Andreas system, California. *Tectonophysics*, *295*(1–2), 199–221. https://doi.org/10.1016/S0040-1951(98)00121-8

Cocco, M., & Tinti, E. (2008). Scale dependence in the dynamics of earthquake propagation: Evidence from seismological and geological observations. *Earth and Planetary Science Letters*, *273*(1–2), 123–131. https://doi.org/10.1016/j.epsl.2008.06.025

Cocco, M., Tinti, E., & Cirella, A. (2016). On the scale dependence of earthquake stress drop. *Journal of Seismology*, *20*(4), 1151–1170. https://doi.org/10.1007/s10950-016-9594-4

Cornelio, C., Passelègue, F. X., Spagnuolo, E., Di Toro, G., & Violay, M. (2020). Effect of fluid viscosity on fault reactivation and coseismic weakening. *Journal of Geophysical Research: Solid Earth*, *125*(1), 1–18. https://doi.org/10.1029/2019JB018883

Cornelio, C., Spagnuolo, E., Di Toro, G., Nielsen, S. B., & Violay, M. (2019). Mechanical behaviour of fluid-lubricated faults. *Nature Communications*, *10*(1), 1274. https://doi.org/10.1038/s41467-019-09293-9

Cowan, D. S. (1999). Do faults preserve a record of seismic slip? A field geologist's opinion. *Journal of Structural Geology*, *21*(8), 995–1001. https://doi.org/10.1016/S0191-8141(99)00046-2

Del Gaudio, P., Di Toro, G., Han, R., Hirose, T., Nielsen, S. B., Shimamoto, T., & Cavallo, A. (2009). Frictional melting of peridotite and seismic slip. *Journal of Geophysical Research*, *114*(B6), B06306. https://doi.org/10.1029/2008JB005990

Demurtas, M., Fondriest, M., Balsamo, F., Clemenzi, L., Storti, F., Bistacchi, A., & Di Toro, G. (2016). Structure of a normal seismogenic fault zone in carbonates: The Vado di Corno Fault, Campo Imperatore, Central Apennines (Italy). *Journal of Structural Geology*, *90*, 185–206. https://doi.org/10.1016/j.jsg.2016.08.004

Demurtas, M., Smith, S. A. F., Prior, D. J., Brenker, F. E., & Di Toro, G. (2019). Grain size sensitive creep during simulated seismic slip in nanogranular fault gouges: Constraints from transmission Kikuchi diffraction (TKD). *Journal of Geophysical Research: Solid Earth*, *124*(10), 10197–10209. https://doi.org/10.1029/2019JB018071

De Paola, N., Holdsworth, R. E., Viti, C., Collettini, C., & Bullock, R. (2015). Can grain size sensitive flow lubricate faults during the initial stages of earthquake propagation? *Earth and Planetary Science Letters*, *431*, 48–58. https://doi.org/10.1016/j.epsl.2015.09.002

Dieterich, J. H., & Kilgore, B. D. (1994). Direct observation of frictional contacts: New insights for state-dependent properties. *Pure and Applied Geophysics PAGEOPH*, *143*(1–3), 283–302. https://doi.org/10.1007/BF00874332

Di Toro, G., Han, R., Hirose, T., De Paola, N., Nielsen, S. B., Mizoguchi, K., et al. (2011). Fault lubrication during earthquakes. *Nature*, *471*(7339), 494–498. https://doi.org/10.1038/nature09838

Di Toro, G., Hirose, T., Nielsen, S. B., Pennacchioni, G., & Shimamoto, T. (2006). Natural and experimental evidence of melt lubrication of faults during earthquakes. *Science*, *311*(5761), 647–649. https://doi.org/10.1126/science.1121012

Di Toro, G., Hirose, T., Nielsen, S. B., & Shimamoto, T. (2006). Relating high-velocity rock-friction experiments to coseismic slip in the presence of melts. *Geophysical Monograph Series*, *170*(March 2014), 121–134. https://doi.org/10.1029/170GM13

Di Toro, G., Niemeijer, A. R., Tripoli, A., Nielsen, S. B., Di Felice, F., Scarlato, P., et al. (2010). From field geology to earthquake simulation: A new state-of-The-art tool to investigate rock friction during the seismic cycle (SHIVA). In *Rendiconti Lincei* (Vol. 21, pp. 95–114). Springer Verlag Italia s.r.l. https://doi.org/10.1007/s12210-010-0097-x

Di Toro, G., & Pennacchioni, G. (2004). Superheated friction-induced melts in zoned pseudotachylytes within the Adamello tonalites (Italian Southern Alps). *Journal of Structural Geology*, *26*(10), 1783–1801. https://doi.org/10.1016/j.jsg.2004.03.001

Di Toro, G., Pennacchioni, G., & Teza, G. (2005). Can pseudotachylytes be used to infer earthquake source parameters? An example of limitations in the study of exhumed faults. *Tectonophysics*, *402*(1–4), 3–20. https://doi.org/10.1016/j.tecto.2004.10.014

Evans, B., & Goetze, C. (1979). The temperature variation of hardness of olivine and its implication for polycrystalline yield stress. *Journal of Geophysical Research*, *84*(B10), 5505. https://doi.org/10.1029/JB084iB10p05505

Faulkner, D. R., Mitchell, T. M., Behnsen, J., Hirose, T., & Shimamoto, T. (2011). Stuck in the Mud? Earthquake nucleation and propagation through accretionary forearcs. *Geophysical Research Letters*, *38*(18), L18303. https://doi.org/10.1029/2011GL048552

Faulkner, D. R., Sanchez-Roa, C., Boulton, C., & den Hartog, S. A. M. (2018). Pore fluid pressure development in compacting fault gouge in theory, experiments, and nature. *Journal of Geophysical Research: Solid Earth*, *123*(1), 226–241. https://doi.org/10.1002/2017JB015130

Ferri, F., Di Toro, G., Hirose, T., & Shimamoto, T. (2010). Evidence of thermal pressurization in high-velocity friction experiments on smectite-rich gouges: Thermal pressurization of clay-rich gouges. *Terra Nova*, *22*(5), 347–353. https://doi.org/10.1111/j.1365-3121.2010.00955.x

Fialko, Y., & Khazan, Y. (2005). Fusion by earthquake fault friction: Stick or slip? *Journal of Geophysical Research*, *110*(B12), B12407. https://doi.org/10.1029/2005JB003869

Gabriel, A.-A., Ampuero, J. P., Dalguer, L. A., & Mai, P. M. (2012). The transition of dynamic rupture styles in elastic media under velocity-weakening friction. *Journal of Geophysical Research*, *117*(B9), B09311. https://doi.org/10.1029/2012JB009468

Giordano, D., Russell, J. K., & Dingwell, D. B. (2008). Viscosity of magmatic liquids: A model. *Earth and Planetary Science Letters*, *271*(1–4), 123–134. https://doi.org/10.1016/j.epsl.2008.03.038

Goldsby, D. L., & Tullis, T. E. (2011). Flash heating leads to low frictional strength of crustal rocks at earthquake slip rates. *Science*, *334*(6053), 216–218. https://doi.org/10.1126/science.1207902

Green, H. W., II, Shi, F., Bozhilov, K., Xia, G., & Reches, Z. (2015). Phase transformation and nanometric flow cause extreme weakening during fault slip. *Nature Geoscience*, *8*(6), 484–489. https://doi.org/10.1038/ngeo2436

Han, R., Hirose, T., & Shimamoto, T. (2010). Strong velocity weakening and powder lubrication of simulated carbonate faults at seismic slip rates. *Journal of Geophysical Research*, *115*(B3), B03412. https://doi.org/10.1029/2008JB006136

Han, R., Shimamoto, T., Hirose, T., Ree, J.-H., & Ando, J.-i. (2007). Ultralow friction of carbonate faults caused by thermal decomposition. *Science*, *316*(5826), 878–881. https://doi.org/10.1126/science.1139763

Harbord, C., Brantut, N., Spagnuolo, E., & Di Toro, G. (2021). Fault Friction during simulated seismic slip pulses. *Journal of Geophysical Research: Solid Earth*, *126*(8), e2021JB022149. https://doi.org/10.1029/2021JB022149

Hartlieb, P., Toifl, M., Kuchar, F., Meisels, R., & Antretter, T. (2016). Thermo-physical properties of selected hard rocks and their relation to microwave-assisted comminution. *Minerals Engineering*, *91*, 34–41. https://doi.org/10.1016/j.mineng.2015.11.008

Heaton, T. H. (1990). Evidence for and implications of self-healing pulses of slip in earthquake rupture. *Physics of the Earth and Planetary Interiors*, *64*(1), 1–20. https://doi.org/10.1016/0031-9201(90)90002-F

Hirose, T., & Shimamoto, T. (2005). Growth of molten zone as a mechanism of slip weakening of simulated faults in gabbro during frictional melting. *Journal of Geophysical Research*, *110*(B5), B05202. https://doi.org/10.1029/2004JB003207

Hung, C.-C., Kuo, L.-W., Spagnuolo, E., Wang, C.-C., Di Toro, G., Wu, W.-J., et al. (2019). Grain fragmentation and frictional melting during initial experimental deformation and implications for seismic slip at shallow depths. *Journal of Geophysical Research: Solid Earth*, *124*(11), 11150–11169. https://doi.org/10.1029/2019JB017905

Italiano, F., Martinelli, G., & Plescia, P. (2008). CO_2 degassing over seismic areas: The role of Mechanochemical production at the study case of Central Apennines BT. In N. M. Pérez, S. Gurrieri, C.-Y. King, & Y. Taran (Eds.) *Terrestrial fluids, earthquakes and volcanoes: The Hiroshi Wakita volume III*, (pp. 75–94). Birkhäuser Basel. https://doi.org/10.1007/978-3-7643-8738-9_6

Kuo, L.-W., Li, H., Smith, S. A. F., Di Toro, G., Suppe, J., Song, S.-R., et al. (2014). Gouge graphitization and dynamic fault weakening during the 2008 Mw 7.9 Wenchuan earthquake. *Geology*, *42*(1), 47–50. https://doi.org/10.1130/G34862.1

Martinelli, G., & Plescia, P. (2004). Mechanochemical dissociation of calcium carbonate: Laboratory data and relation to natural emissions of CO_2. *Physics of the Earth and Planetary Interiors*, *142*(3–4), 205–214. https://doi.org/10.1016/j.pepi.2003.12.009

Masoch, S., Fondriest, M., Preto, N., Secco, M., & Di Toro, G. (2019). Seismic cycle recorded in cockade-bearing faults (Col de Teghime, Alpine Corsica). *Journal of Structural Geology*, *129*, 103889. https://doi.org/10.1016/j.jsg.2019.103889

Merriman, J. D., Hofmeister, A. M., Roy, D. J., & Whittington, A. G. (2018). Temperature-dependent thermal transport properties of carbonate minerals and rocks. *Geosphere*, *14*(4), 1961–1987. https://doi.org/10.1130/GES01581.1

Miao, S. Q., Li, H. P., & Chen, G. (2014). Temperature dependence of thermal diffusivity, specific heat capacity, and thermal conductivity for several types of rocks. *Journal of Thermal Analysis and Calorimetry*, *115*(2), 1057–1063. https://doi.org/10.1007/s10973-013-3427-2

Murphy, S., Di Toro, G., Romano, F., Scala, A., Lorito, S., Spagnuolo, E., et al. (2018). Tsunamigenic earthquake simulations using experimentally derived friction laws. *Earth and Planetary Science Letters*, *486*, 155–165. https://doi.org/10.1016/j.epsl.2018.01.011

Nielsen, S. B., Di Toro, G., & Griffith, W. A. (2010). Friction and roughness of a melting rock surface. *Geophysical Journal International*, *182*(1), 299–310. https://doi.org/10.1111/j.1365-246X.2010.04607.x

Nielsen, S. B., Di Toro, G., Hirose, T., & Shimamoto, T. (2008). Frictional melt and seismic slip. *Journal of Geophysical Research*, *113*(B1), B01308. https://doi.org/10.1029/2007JB005122

Nielsen, S. B., Mosca, P., Giberti, G., Di Toro, G., Hirose, T., & Shimamoto, T. (2010). On the transient behavior of frictional melt during seismic slip. *Journal of Geophysical Research*, *115*(10), B10301. https://doi.org/10.1029/2009JB007020

Nielsen, S. B., Spagnuolo, E., Violay, M., & Di Toro, G. (2021). Thermal weakening friction during seismic slip: Experiments and models with heat sources and sinks. *Journal of Geophysical Research: Solid Earth*, *126*(5), e2020JB020652. https://doi.org/10.1029/2020JB020652

Nielsen, S. B., Spagnuolo, E., Violay, M., Smith, S. A. F., Di Toro, G., & Bistacchi, A. (2016). G: Fracture energy, friction and dissipation in earthquakes. *Journal of Seismology*, *20*(4), 1187–1205. https://doi.org/10.1007/s10950-016-9560-1

Niemeijer, A. R., Di Toro, G., Nielsen, S. B., & Di Felice, F. (2011). Frictional melting of gabbro under extreme experimental conditions of normal stress, acceleration, and sliding velocity. *Journal of Geophysical Research*, *116*(7), B07404. https://doi.org/10.1029/2010JB008181

Noda, H. (2008). Frictional constitutive law at intermediate slip rates accounting for flash heating and thermally activated slip process. *Journal of Geophysical Research*, *113*(B9), B09302. https://doi.org/10.1029/2007JB005406

Noda, H., & Lapusta, N. (2013). Stable creeping fault segments can become destructive as a result of dynamic weakening. *Nature*, *493*(7433), 518–521. https://doi.org/10.1038/nature11703

Nunez Cascajero, A., Tapetado, A., & Vazquez, C. (2021). High spatial resolution optical fiber two color pyrometer with fast response. *IEEE Sensors Journal*, *21*(3), 2942–2950. https://doi.org/10.1109/JSEN.2020.3022179

Papa, S., Spagnuolo, E., Di Toro, G., Cavallo, A., Favero, M., Camacho, A., & Pennacchioni, G. (2021). Selective clast survival in an experimentally-produced pseudotachylyte. *Journal of Structural Geology*, *147*(December 2020), 104328. https://doi.org/10.1016/j.jsg.2021.104328

Passelègue, F. X., Goldsby, D. L., & Fabbri, O. (2014). The influence of ambient fault temperature on flash-heating phenomena. *Geophysical Research Letters*, *41*(3), 828–835. https://doi.org/10.1002/2013GL058374

Passelègue, F. X., Schubnel, A., Nielsen, S. B., Bhat, H. S., Deldicque, D., & Madariaga, R. (2016). Dynamic rupture processes inferred from laboratory microearthquakes. *Journal of Geophysical Research: Solid Earth*, *121*(6), 4343–4365. https://doi.org/10.1002/2015JB012694

Passelègue, F. X., Spagnuolo, E., Violay, M., Nielsen, S. B., Di Toro, G., & Schubnel, A. (2016). Frictional evolution, acoustic emissions activity, and off-fault damage in simulated faults sheared at seismic slip rates. *Journal of Geophysical Research: Solid Earth*, *121*(10), 7490–7513. https://doi.org/10.1002/2016JB012988

Persson, B. N. J. (2006). Contact mechanics for randomly rough surfaces. *Surface Science Reports*, *61*(4), 201–227. https://doi.org/10.1016/j.surfrep.2006.04.001

Platt, J. D., Brantut, N., & Rice, J. R. (2015). Strain localization driven by thermal decomposition during seismic shear. *Journal of Geophysical Research: Solid Earth*, *120*(6), 4405–4433. https://doi.org/10.1002/2014JB011493

Poirier, J. P. (1995). *Plastic rheology of crystals*. Mineral Physics & Crystallography. https://doi.org/10.1029/RF002p0237

Pozzi, G., De Paola, N., Holdsworth, R. E., Bowen, L., Nielsen, S. B., & Dempsey, E. D. (2019). Coseismic ultramylonites: An investigation of nanoscale viscous flow and fault weakening during seismic slip. *Earth and Planetary Science Letters*, *516*, 164–175. https://doi.org/10.1016/j.epsl.2019.03.042

Pozzi, G., De Paola, N., Nielsen, S. B., Holdsworth, R. E., & Bowen, L. (2018). A new interpretation for the nature and significance of mirror-like surfaces in experimental carbonate-hosted seismic faults. *Geology*, *46*(7), 583–586. https://doi.org/10.1130/G40197.1

Pozzi, G., De Paola, N., Nielsen, S. B., Holdsworth, R. E., Tesei, T., Thieme, M., & Demouchy, S. (2021). Coseismic fault lubrication by viscous deformation. *Nature Geoscience*, *14*(6), 437–442. https://doi.org/10.1038/s41561-021-00747-8

Proctor, B. P., Mitchell, T. M., Hirth, G., Goldsby, D., Zorzi, F., Platt, J. D., & Di Toro, G. (2014). Dynamic weakening of serpentinite gouges and bare surfaces at seismic slip rates. *Journal of Geophysical Research: Solid Earth*, *119*(11), 8107–8131. https://doi.org/10.1002/2014JB011057

Reches, Z., & Lockner, D. A. (2010). Fault weakening and earthquake instability by powder lubrication. *Nature*, *467*(7314), 452–455. https://doi.org/10.1038/nature09348

Rempel, A. W., & Weaver, S. L. (2008). A model for flash weakening by asperity melting during high-speed earthquake slip. *Journal of Geophysical Research*, *113*(B11), B11308. https://doi.org/10.1029/2008JB005649

Rice, J. R. (1999). Flash heating at asperity contacts and rate-dependent friction. *Eos Trans. AGU*, *80*(46), F471.

Rice, J. R. (2006). Heating and weakening of faults during earthquake slip. *Journal of Geophysical Research*, *111*(5), B05311. https://doi.org/10.1029/2005JB004006

Rice, J. R., & Cocco, M. (2007). Seismic fault rheology and earthquake dynamics. *Tectonic Faults: Agents of Change on a Dynamic Earth*, 16–21. Retrieved from http://www.geophysik.uni-muenchen.de/~malservisi/LITHO/papers/RiceCocco_DahlemWrkshp05.pdf

Rodriguez-Navarro, C., Kudlacz, K., & Ruiz-Agudo, E. (2012). The mechanism of thermal decomposition of dolomite: New insights from 2D-XRD and TEM analyses. *American Mineralogist*, *97*(1), 38–51. https://doi.org/10.2138/am.2011.3813

Rodriguez-Navarro, C., Ruiz-Agudo, E., Luque, A., Rodriguez-Navarro, A. B., & Ortega-Huertas, M. (2009). Thermal decomposition of calcite: Mechanisms of formation and textural evolution of CaO nanocrystals. *American Mineralogist*, *94*(4), 578–593. https://doi.org/10.2138/am.2009.3021

Rowe, C. D., & Griffith, W. A. (2015). Do faults preserve a record of seismic slip: A second opinion. *Journal of Structural Geology*, *78*, 1–26. https://doi.org/10.1016/j.jsg.2015.06.006

Rowe, C. D., Lamothe, K., Rempe, M., Andrews, M., Mitchell, T. M., Di Toro, G., et al. (2019). Earthquake lubrication and healing explained by amorphous nanosilica. *Nature Communications*, *10*(1), 320. https://doi.org/10.1038/s41467-018-08238-y

Rutter, E. H. (1972). The influence of interstitial water on the rheological behaviour of calcite rocks. *Tectonophysics*, *14*(1), 13–33. https://doi.org/10.1016/0040-1951(72)90003-0

Sammis, C. G., & Ben-Zion, Y. (2008). Mechanics of grain-size reduction in fault zones. *Journal of Geophysical Research*, *113*(B2), B02306. https://doi.org/10.1029/2006JB004892

Schmid, S. M., Boland, J. N., & Paterson, M. S. (1977). Superplastic flow in finegrained limestone. *Tectonophysics*, *43*(3–4), 257–291. https://doi.org/10.1016/0040-1951(77)90120-2

Schmid, S. M., Panozzo, R., & Bauer, S. (1987). Simple shear experiments on calcite rocks: Rheology and microfabric. *Journal of Structural Geology*, *9*(5), 747–778. https://doi.org/10.1016/0191-8141(87)90157-X

Shimamoto, T., & Tsutsumi, A. (1994). A new rotary-shear high-speed frictional testing machine: Its basic design and scope of research. *Journal of Tectonic Research Group Japan*, *39*, 65–78.

Sibson, R. H. (1973). Interactions between temperature and pore-fluid pressure during earthquake faulting and a mechanism for partial or total stress relief. *Nature Physical Science*, *243*(126), 66–68. https://doi.org/10.1038/physci243066a0

Sibson, R. H. (1975). Generation of pseudotachylyte by ancient seismic faulting. *Geophysical Journal of the Royal Astronomical Society*, *43*(3), 775–794. https://doi.org/10.1111/j.1365-246X.1975.tb06195.x

Sibson, R. H. (2003). Thickness of the seismic slip zone. *Bulletin of the Seismological Society of America*, *93*(3), 1169–1178. https://doi.org/10.1785/0120020061

Sibson, R. H., Moore, J. M. M., & Rankin, A. H. (1975). Seismic pumping—A hydrothermal fluid transport mechanism. *Journal of the Geological Society*, *131*(6), 653–659. https://doi.org/10.1144/gsjgs.131.6.0653

Siman-Tov, S., Aharonov, E., Sagy, A., & Emmanuel, S. (2013). Nanograins form carbonate fault mirrors. *Geology*, *41*(6), 703–706. https://doi.org/10.1130/G34087.1

Smith, S. A. F., Nielsen, S. B., & Di Toro, G. (2015). Strain localization and the onset of dynamic weakening in calcite fault gouge. *Earth and Planetary Science Letters*, *413*, 25–36. https://doi.org/10.1016/j.epsl.2014.12.043

Sorensen, D. C. (1982). Newton's method with a model trust region Modification. *SIAM Journal on Numerical Analysis*, *19*(2), 409–426. https://doi.org/10.1137/0719026

Spagnuolo, E., Plümper, O., Violay, M., Cavallo, A., & Di Toro, G. (2015). Fast-moving dislocations trigger flash weakening in carbonate-bearing faults during earthquakes. *Scientific Reports*, *5*(1), 16112. https://doi.org/10.1038/srep16112

Spray, J. G. (1995). Pseudotachylyte controversy: Fact or friction? *Geology*, *23*(12), 1119–1122. https://doi.org/10.1130/0091-7613(1995)023<1119:PCFOF>2.3.CO;2

Spray, J. G. (2010). Frictional melting processes in planetary materials: From hypervelocity impact to earthquakes. *Annual Review of Earth and Planetary Sciences*, *38*(1), 221–254. https://doi.org/10.1146/annurev.earth.031208.100045

Sulem, J., & Famin, V. (2009). Thermal decomposition of carbonates in fault zones: Slip-weakening and temperature-limiting effects. *Journal of Geophysical Research*, *114*(3), 1–14. https://doi.org/10.1029/2008jb006004

Tinti, E., Bizzarri, A., & Cocco, M. (2005). Modeling the dynamic rupture propagation on heterogeneous faults with rate- and state-dependent friction. *Annals of Geophysics*, *48*(2), 327–345. https://doi.org/10.4401/ag-3205

Tinti, E., Casarotti, E., Ulrich, T., Taufiqurrahman, T., Li, D., & Gabriel, A.-A. (2021). Constraining families of dynamic models using geological, geodetic and strong ground motion data: The Mw 6.5, October 30th, 2016, Norcia earthquake, Italy. *Earth and Planetary Science Letters*, *576*, 117237. https://doi.org/10.1016/j.epsl.2021.117237

Tisato, N., Di Toro, G., De Rossi, N., Quaresimin, M., & Candela, T. (2012). Experimental investigation of flash weakening in limestone. *Journal of Structural Geology*, *38*, 183–199. https://doi.org/10.1016/j.jsg.2011.11.017

Tsutsumi, A., & Shimamoto, T. (1997). High-velocity frictional properties of gabbro. *Geophysical Research Letters*, *24*(6), 699–702. https://doi.org/10.1029/97GL00503

Tullis, T. E. (2015). Mechanisms for friction of rock at earthquake slip rates. In *Treatise on Geophysics* (2nd edn., pp. 131–152).

Verberne, B. A., Plümper, O., De Winter, D. A. M., & Spiers, C. J. (2014). Superplastic nanofibrous slip zones control seismogenic fault friction. *Science*, *346*(6215), 1342–1344. https://doi.org/10.1126/science.1259003

Violay, M., Di Toro, G., Nielsen, S. B., Spagnuolo, E., & Burg, J. P. (2015). Thermo-mechanical pressurization of experimental faults in cohesive rocks during seismic slip. *Earth and Planetary Science Letters*, *429*, 1–10. https://doi.org/10.1016/j.epsl.2015.07.054

Violay, M., Nielsen, S. B., Gibert, B., Spagnuolo, E., Cavallo, A., Azais, P., et al. (2014). Effect of water on the frictional behavior of cohesive rocks during earthquakes. *Geology*, *42*(1), 27–30. https://doi.org/10.1130/G34916.1

Violay, M., Passelegue, F., Spagnuolo, E., Di Toro, G., & Cornelio, C. (2019). Effect of water and rock composition on re-strengthening of cohesive faults during the deceleration phase of seismic slip pulses. *Earth and Planetary Science Letters*, *522*, 55–64. https://doi.org/10.1016/j.epsl.2019.06.027

References From the Supporting Information

Badt, N. Z., Tullis, T. E., Hirth, G., & Goldsby, D. L. (2020). Thermal pressurization weakening in laboratory experiments. *Journal of Geophysical Research: Solid Earth*, *125*(5), e2019JB018872. https://doi.org/10.1029/2019jb018872

Bizzarri, A., & Cocco, M. (2006). A thermal pressurization model for the spontaneous dynamic rupture propagation on a three-dimensional fault: 2. Traction evolution and dynamic parameters. *Journal of Geophysical Research*, *111*(B5), B05304. https://doi.org/10.1029/2005JB003864

Brantut, N., & Mitchell, T. M. (2018). Assessing the efficiency of thermal pressurization using natural pseudotachylyte-bearing rocks. *Geophysical Research Letters*, *45*(18), 9533–9541. https://doi.org/10.1029/2018GL078649

Garagash, D. I., & Germanovich, L. N. (2012). Nucleation and arrest of dynamic slip on a pressurized fault. *Journal of Geophysical Research B: Solid Earth*, *117*(10), B10310. https://doi.org/10.1029/2012JB009209

Nadeau, R. M., & Johnson, L. R. (1998). Seismological studies at Parkfield VI: Moment release rates and estimates of source parameters for small repeating earthquakes. *Bulletin of the Seismological Society of America*, *88*(3), 790–814.

Rempel, A. W., & Rice, J. R. (2006). Thermal pressurization and onset of melting in fault zones. *Journal of Geophysical Research*, *111*(B9), B09314. https://doi.org/10.1029/2006JB004314

Viesca, R. C., & Garagash, D. I. (2015). Ubiquitous weakening of faults due to thermal pressurization. *Nature Geoscience*, *8*(11), 875–879. https://doi.org/10.1038/ngeo2554

Vinciguerra, S., Trovato, C., Meredith, P. G., & Benson, P. M. (2005). Relating seismic velocities, thermal cracking and permeability in Mt. Etna and Iceland basalts. *International Journal of Rock Mechanics and Mining Sciences*, *42*(7–8), 900–910. https://doi.org/10.1016/j.ijrmms.2005.05.022

Wibberley, C. A. J., & Shimamoto, T. (2005). Earthquake slip weakening and asperities explained by thermal pressurization. *Nature*, *436*(7051), 689–692. https://doi.org/10.1038/nature03901